Subsurface Eddy Detection Optimized with Potential Vorticity from Models in the Arabian Sea

Paul Ernst, Bulusu Subrahmanyam, Yves Morel, Corinne Trott, Alexis Chaigneau

Subsurface Eddy Detection Optimized with Potential Vorticity from Models in the Arabian Sea

Paul A. Ernst,[a] Bulusu Subrahmanyam,[a] Yves Morel,[b] Corinne B. Trott,[c] and Alexis Chaigneau[b]

[a] *School of the Earth, Ocean, and Environment, University of South Carolina, Columbia, SC 29208*

[b] *LEGOS, Université de Toulouse, CNES, CNRS, IRD, UPS, Toulouse, France*

[c] *Naval Research Laboratory, Stennis Space Center, MS 39529*

Corresponding author: Paul A. Ernst, pernst@seoe.sc.edu

ABSTRACT

Coherent ocean vortices, or eddies, are usually tracked on the surface of the ocean. However, tracking subsurface eddies is important for a complete understanding of deep ocean circulation. In this study, we develop an algorithm designed for the detection of subsurface eddies in the Arabian Sea using Nucleus for European Modelling of the Ocean (NEMO) model simulations. We optimize each parameter of our algorithm to achieve favorable results when compared with an algorithm using sea surface height (SSH). When compared to similar methods, we find that using the rescaled isopycnal potential vorticity (PV) is best for subsurface eddy detection. We proceed to demonstrate that our new algorithm can detect eddies successfully between specific isopycnals, such as those that define the Red Sea Water (RSW). In doing so, we showcase how our method can be used to describe the properties of eddies within the RSW and even identify specific long-lived subsurface eddies. We conduct one such case study by discerning the structure of a completely subsurface RSW eddy near the Chagos Archipelago using Lagrangian particle tracking and PV diagnostics. We conclude that our rescaled PV method is an efficient tool for investigating eddy dynamics within the ocean's interior, and publicly provide our optimization methodology as a way for other researchers to develop their own subsurface detection algorithms with optimized parameters for any spatiotemporal model domain.

SIGNIFICANCE STATEMENT

Eddies are a key part of ocean circulation both at the surface and in the subsurface. The purpose of our study was to design the first detection method comprehensively optimized for subsurface eddy detection from numerical simulations. We demonstrate that potential vorticity (PV) is the best field to use when algorithmically tracking eddies in subsurface water masses, using our new method to identify and track eddies in the Red Sea Water (RSW). Additionally, our method allows us to efficiently evaluate the dynamics of eddies through potential vorticity diagnostics, exemplified with a previously undescribed eddy near the Chagos Archipelago. Our methodology can be used by future researchers to study the eddy dynamics hidden within subsurface water masses around the world.

1. Introduction

Coherent ocean vortices known as eddies are ubiquitous throughout the world's oceans (Chelton et al., 2011). Mesoscale (50-300 km) eddies contribute as much to global mass transport as the mean flow (Zhang et al., 2014). In the Arabian Sea, the variability of the surface mesoscale eddy field is primarily driven by instability generated via the seasonal reversal of monsoon winds, producing the southwest monsoon in the summer and northeast monsoon in the winter (Trott et al., 2018). As a result of the reversing winds and their associated planetary wave dynamics, several climatological eddies consistently form in the same regions every year, including the Great Whirl and the Socotra Eddy in the Somali Current region, as well as the Lakshadweep High in the Laccadive Sea (Beal and Donohue, 2013; Ernst et al., 2022; Shankar and Shetye, 1997). These named eddies and the mesoscale eddy field as a whole modulate changes in upper ocean stratification, air-sea interactions, and transport of heat and salt across the Arabian Sea (Trott et al., 2019; Wang et al., 2019; Zhan et al., 2020).

Oceanic eddies and their impacts are often studied with the aid of automated eddy detection and tracking algorithms due to their transience, ubiquity, and the increasing number of observations (Lian et al., 2019). At the surface, the most widely used detection methods utilize quantities derived from sea surface height (SSH), including sea level anomaly (SLA), absolute dynamic topography (ADT), and geostrophic currents (Chaigneau et al., 2008; Pegliasco et al., 2021; Nencioli et al., 2010). Currents in particular may be further processed to derive other fields through which eddies can be identified, including relative vorticity, the Okubo-Weiss (OW) parameter, and the local normalized angular momentum (LNAM) (Isern-Fontanet et al., 2003; Le Vu et al., 2018; Souza et al., 2011). Conventional Eulerian algorithms use these fields to identify local extremes that correspond with eddy centers, as well as numerical or geometric criteria that define eddy edges (Sadarjoen and Post, 2000). By contrast, Lagrangian methods, including the Lagrangian averaged vorticity deviation and the modulus of vorticity, define Lagrangian coherent structures (LCS) associated with the attraction or repulsion of particles (Haller et al., 2019; Vortmeyer-Kley et al., 2016, 2019). Generally, Lagrangian methods tend to detect fewer total eddies with smaller eddy radii, being highly sensitive to the time integration parameter while adhering to a stricter definition of particle interactions (Vortmeyer-Kley et al., 2019). Both Eulerian and Lagrangian methods have been compared for surface mesoscale eddy detection, with the prevailing conclusion that different

algorithms are suitable for different purposes, although some methods conclusively perform better than others at specific tasks (Lian et al., 2019; Souza et al., 2011; Vortmeyer-Kley et al., 2019).

While eddy detection and tracking at the surface has been extensively developed, subsurface eddy detection in both observations and models is less mature. High resolution satellite data are only available at the surface, meaning that subsurface data must be derived from numerical models, synthetic profiles, or sparse *in-situ* observations (Petersen et al., 2013). In the first two cases, verification of completely subsurface findings is scarce; while in the third case, observations can provide a limited picture of eddy three-dimensional structure and occasionally identify individual subsurface eddies, but ultimately cannot provide a comprehensive overview of subsurface eddying (Assassi et al., 2016; de Marez et al., 2019; de Marez et al., 2020; Sun et al., 2022). Regardless, models have been used for subsurface eddy surveys in the past, albeit using methodologies and thresholds developed for surface eddy detection or using algorithms that compare unfavorably with more recently developed methodologies (Doglioli et al., 2007; Petersen et al., 2013; Lian et al., 2019; Xu et al., 2019). Due to the lack of SSH and corresponding geostrophic current measurements found beneath the surface, methodologies need to be adapted and optimized for a subsurface ageostrophic environment. Many of the best-performing methodologies were designed using criteria derived for geostrophic regimes, such as edge detection methods that require finding closed streamlines (Le Vu et al., 2018; Nencioli et al., 2010). Therefore, there is a current lack of synchronicity between existing surface and potential subsurface eddy detection algorithms.

Successful subsurface tracking methodologies, properly implemented, may be used for multiple purposes, including the study of the spread of distinct water masses. In the Arabian Sea, there are several high-salinity water masses that typically exist in the range between 0 and 1000 meters: the Arabian Sea high salinity water (ASHSW), Persian Gulf water (PGW), and Red Sea water (RSW) (Prasad et al., 2001). These water masses each impact the physical structure of the Arabian Sea with implications for oxygen and nutrient concentrations both above and below the pycnocline (Morrison et al., 1998; Queste et al., 2018). Recent modelling and observational studies have indicated the role that subsurface eddies might play in the spreading and mixing of these water masses (L'Hégaret et al., 2015, 2016, 2021; Morvan et al., 2020). L'Hégaret et al. (2021) specifically suggest that mesoscale eddies have a major impact on the distribution and spreading of outflows from the Gulf of Oman and Gulf of Aden

(GoA) through the rest of the Arabian Sea. Through the development of a specialized eddy tracking algorithm, we aim to distribute a tool that can efficiently detect eddies that lie specifically within important subsurface water masses. Here, we choose RSW as an example due to its identifiable presence at depths greater than 600 meters (L'Hégaret et al. 2021).

Eddy detection algorithms aimed at detecting purely subsurface eddies must perform well independently from surface-derived measurements. The main remaining model-derived fields for use are current velocities, temperature, and salinity. From these, vorticity, the OW parameter, and LNAM are all viable derived fields. PV is another useful field for use in subsurface eddy detection, and has been used to success observationally but is more complex for surface eddy tracking due to the effect of outcropping (Bretherton, 1966; Morel et al., 2019; Pelland et al., 2013; Schneider et al., 2003). In this study, we will perform the first comparison and optimization of Eulerian subsurface eddy detection algorithms derived from these fields against an established winding angle algorithm using SSH at the surface (Chaigneau et al., 2008). We will then demonstrate our resulting optimized algorithm by characterizing the dynamics of a large, previously undiscovered subsurface eddy that forms semi-regularly to the east of the Chagos Archipelago. The remainder of our study is organized as follows: section 2 details the data, fields, and tracking algorithm used in this study, section 3 describes the optimization of our algorithms, section 4 is a case study of a subsurface eddy that highlights the effectiveness of our optimized algorithm, and section 5 presents a summary and the conclusions of our work.

2. Data & Methodology

a. Model Simulations

In this study, we use model simulations from the Nucleus for the European Modelling of the Ocean (NEMOv3.1) maintained by the Copernicus Marine Environmental Service (CMEMS), available online at https://resources.marine.copernicus.eu/ with a product ID of GLOBAL_ANALYSIS_FORECAST_PHY_001_024. Variables used include potential temperature and salinity from which we derive potential density, SSH, and zonal and meridional velocities. This is a daily gridded 1/12º horizontal resolution dataset with 50 vertical levels between 0 meters and 5500 meters. Output is generated in 10-day forecast segments beginning on January 1st, 2016 and extending into 2022. We choose this model simulations

given its eddy-resolving high resolution and the fact that it has been successfully used in studies of Indian Ocean dynamics, notably in the Bay of Bengal (Roman-Stork and Subrahmanyam, 2020). As these are publicly available model outputs, the use of this product in this study allows for reproduction of our results and calibration of other subsurface eddy detection methodologies in the future.

b. Field Calculations

1) VORTICITY

We calculate relative vorticity, ω, as the curl of the total velocity field:

$$\boldsymbol{\omega} = \frac{\partial \boldsymbol{v}}{\partial \boldsymbol{x}} - \frac{\partial \boldsymbol{u}}{\partial \boldsymbol{y}}, \tag{1}$$

where v and u are the magnitudes of the meridional and zonal currents respectively. In the northern hemisphere, a high-magnitude positive vorticity indicates a maximum of cyclonic rotation, while a high-magnitude negative vorticity indicates a maximum of anticyclonic rotation. Vorticity typically decreases from a maximum at the eddy center to zero in the area of maximum velocity of an isolated eddy, then often reverses sign towards its outer edge (Aouni, 2021).

2) OKUBO-WEISS PARAMETER

The Okubo-Weiss (OW) parameter, W, is a combination of vorticity as well as the normal (s_n) and shear (s_s) components of the strain as follows (Okubo, 1970; Weiss, 1991):

$$\boldsymbol{s_n} = \frac{\partial \boldsymbol{u}}{\partial \boldsymbol{x}} - \frac{\partial \boldsymbol{v}}{\partial \boldsymbol{y}}, \tag{2}$$

$$s_s = \frac{\partial v}{\partial x} + \frac{\partial u}{\partial y}, \tag{3}$$

and

$$\boldsymbol{W} = \boldsymbol{s_n^2} + \boldsymbol{s_s^2} - \boldsymbol{\omega^2}. \tag{4}$$

A highly negative W signifies a vorticity dominated environment, indicating a likely eddy center, and W increases towards the edge of an eddy. The sign of the relative vorticity in the eddy center is used to determine the sense of rotation of an eddy detected using the OW parameter.

3) Local Normalized Angular Momentum

The local normalized angular momentum (LNAM) is defined identically to Le Vu et al. (2018)'s Eq. (2) as implemented in their Angular Momentum Eddy Detection Algorithm (AMEDA):

$$\mathbf{LNAM}(\boldsymbol{G_i}) = \frac{\sum_j \boldsymbol{G_i X_j} \times \boldsymbol{V_j}}{\sum_j \boldsymbol{G_i X_j}\, \boldsymbol{V_j} + \sum_j \left|\boldsymbol{G_i X_j}\right| \left|\boldsymbol{V_j}\right|} = \frac{\boldsymbol{L_i}}{\boldsymbol{S_i} + \mathbf{BL_i}}, \tag{5}$$

Where G_i is a grid point and X_j and V_j are the position and velocity vector of a neighboring point; L_i is therefore the local angular momentum at G_i while S_i, the sum of the scalar products, is added to the renormalization term BL_i. The summed area is a square domain whose exact size depends upon the first baroclinic deformation radius. LNAM is especially useful for detecting eddies whose size lies closely to this radius; as the Arabian Sea lies at low latitudes, this varies from more than 200 km towards the equator to 80 km or less towards the northern terrestrial boundaries (Chelton et al., 1998). The only difference between our formulation of LNAM here and LNAM as defined in Le Vu et al. (2018) is that we use ageostrophic currents in this analysis. A full description of LNAM can be found in Le Vu et al. (2018).

4) Rescaled Potential Vorticity

We calculate the rescaled potential vorticity (PV) as designed by Morel et al. (2019) and demonstrated by Assene et al. (2020). The rescaled PV is defined as

$$\begin{aligned} \mathbf{PV_{rescaled}} &= (\boldsymbol{\nabla} \times \boldsymbol{U} + \boldsymbol{f}).\boldsymbol{\nabla Z}(\boldsymbol{\rho}) \\ &= \mathbf{div}[\,(\boldsymbol{\nabla} \times \boldsymbol{U} + \boldsymbol{f})\boldsymbol{\nabla Z}(\boldsymbol{\rho})\,] \end{aligned} \tag{6}$$

where U is the velocity field, f defines the Coriolis parameter, and $Z(\rho)$ is a function of potential density. In practice, this function is a reference density profile chosen to represent the stratification of an area such that the typically overwhelming signature of the pycnocline in the traditional Ertel PV can be minimized or eliminated. Therefore the choice of this profile depends upon the spatiotemporal study area. While the rescaled PV (hereafter PV) is highly sensitive to the choice of reference profile in the surface layers, it becomes less important the further away the calculation is made from the pycnocline. For this study, we choose a new reference profile located at 72ºE, 0ºN on a particular day for each monsoon for each year: July 1st for the summer monsoon, and January 1st for the winter monsoon. This location on these

dates often displays stratification typical of the open ocean Arabian Sea and rarely contains either eddies or a distinct signature of RSW, making it ideal for the elimination of near-surface stratification without interfering with subsurface water mass signatures.

The rescaled PV bears the same conservation properties as the traditional Ertel PV and is also closely related to the quasigeostrophic PV. As a result, it is more closely related to other dynamical fields, such as vorticity. Indeed, at rest, the rescaled PV is close to f, the local Coriolis parameter, and an eddy can be identified by its PV anomaly (*i.e.* $PVa = \text{PV}-f$) within a layer bounded by two isopycnals, determining its dynamical core. Similarly to quasigeostrophic eddies, the vertical integration of the rescaled PV within this layer is then representative of the eddy strength. Finally, in numerical configurations where tides are simulated, internal gravity waves are generated and they can have a strong mesoscale signature in all dynamical fields (pressure, stratification, velocity, vorticity) that can spoil detection and tracking of eddies. PV filters out the signature of gravity waves, which, even though the present simulation results used here do not represent tides, is another argument for the use of PV for the detection of eddies.

This makes the rescaled PV a powerful tool for interpreting the dynamics of subsurface eddies in numerical models, though some considerations must be noted. Firstly, the necessary use of isopycnic layers separates the calculation of the PV field from the other fields noted here, which are typically calculated at static depths. Secondly, the dynamics associated with PV anomalies are non-local, such that the velocity or vorticity fields associated with a PV anomaly extend outside the layer. The choice of the isopycnal layers is thus crucial and vertical sections can be used to make sure the layer is associated with specific PV signature of water masses and eddies. Finally, when considering the surface layer, the previous arguments are still valid replacing the upper isopycnic surface bounding the layer with the ocean surface. But an additional effect, representing the dynamical effect of outcropping in terms of a PV Dirac sheet, has to be calculated (Bretherton, 1966; Schneider, 2003; Morel et al, 2019). The calculation of the mean isopycnal PV proposed in Assene et al (2020) has here been extended to take this term into account (Bretherton, 1966; Schneider, 2003; Morel et al, 2019). For the optimization component of this study, we calculate the surface layer of the PV between 1000 kg m^{-3} and 1025.5 kg m^{-3}, accounting for this outcropping at the surface (see Appendix). The 1025.5 kg m^{-3} boundary corresponds to the upper edge of the PGW mass as defined by L'Hégaret et al.

(2021). As a result, this isopycnal is effective at capturing the surface water mass dynamics in the Arabian Sea without being contaminated by subsurface dynamics as a denser isopycnal might. Less dense bounding isopycnals reduce the viable study areas around the Gulfs of Aden and Oman due to the highly dense surface water in these locations.

5) VERTICAL VELOCITY

We obtain estimates of vertical velocity (w) using the zonal (u) and meridional (v) components of velocity where appropriate through the integration of the continuity equation:

$$\frac{\partial w}{\partial z} = -\left(\frac{\partial u}{\partial x} + \frac{\partial \mathrm{v}}{\partial \mathrm{y}}\right) \tag{7}$$

c. Eddy Detection Methods

1) THRESHOLDED METHODS

Thresholded methods search for an area with only one local extreme where the largest enclosing contour is at (or sometimes above, depending on the exact formulation) a threshold defined by the field in question. These thresholds can be determined at a fixed value arbitrarily, or as a result of some other calculation. The most common calculation performed to obtain a threshold for OW is as a multiplicative factor of the standard deviation of the field. Hereafter, this multiplier is called the STD factor (*e.g.* Henson & Thomas, 2008; Lian et al., 2019). We will use the standard deviation method, but optimize the STD factor for both OW and vorticity, with the ensuing methods of center and edge detection being labelled hereafter as OW_T and $VORT_T$ respectively. The STD factors of each will differ between center detection and edge detection, as the center factor will be stricter than the edge factor to ensure a local extreme is properly identified. It is worth noting that threshold methods necessarily may not need to obtain centers before enclosing contours. In this study, we separate both in order to determine if different center and edge detection fields or methods are more efficient than a single field center-and-edge detection method.

LNAM as defined by Le Vu et al. (2018) is also a thresholded method with a static parameter K that is specified as $|\mathrm{LNAM}(\mathrm{LOW} < 0)| = K$, where LOW is the Local Okubo Weiss parameter, calculated in the same domain as LNAM. As with the OW_T and $VORT_T$ methods' thresholds, we will optimize K. LNAM is designed and calculated as a center detection method, not as an edge detection method, and so we only use LNAM for obtaining eddy centers.

2) Winding Angle Methods

Winding angle methods are those that do not set a threshold for obtaining eddy centers or edges, instead obtaining these features by searching for the largest closed contour around a single local extreme with at least 4 x 4 grid points enclosed. This is the original methodology used by Chaigneau et al. (2008) with SLA (hereafter referred to as the SSH method, as SSH is the field available in the NEMO model simulations used). We use the winding angle methodology for OW, hereafter OW_{WA}, vorticity, hereafter $VORT_{WA}$, and PV averaged within a layer bounded by two isopycnals, hereafter PV_{ISO}. The only parameter that must be set for winding angle methods is the search increment, which we set as a value lower than the typical absolute minimum value for each respective parameter: 10^{-4} m for SSH, 10^{-7} s^{-1} for $VORT_{WA}$, 10^{-14} s^{-1} for OW_{WA}, and 10^{-7} s^{-1} for PV_{ISO}. As Lian et al., (2019) demonstrate, winding angle methods are weakly sensitive to adjustments in this parameter. Our chosen values, at the expense of longer computation times, ensure that the closed contours we obtain are accurate and do not stop short of the largest closed contour. The winding angle contour edge can be discarded to isolate the winding angle center, allowing for a hybridization of different center and edge detection methodologies as we detail in Section 3.

d. Error-derived Similarity Score

In order to numerically optimize the performance of each prospective subsurface eddy detection method, we employ a metric that we will attempt to maximize as we vary each detection method's parameters. We first recognize that we must perform this optimization at the surface, given the lack of observation-based subsurface eddy identification algorithms. Due to the success of the SSH method in previous studies specifically in the Arabian Sea, we first analyze surface eddies and use this method's output as our benchmark (Ernst et al., 2022; Trott et al., 2018, 2019). Given that our goal is to obtain an algorithm with the best possible similarity to a proven surface detection method at depth, we can compare the output of our methods to the SSH method in several ways. We have selected four axes along which to measure error, selected to reflect the critical components of an eddy tracking algorithm: number of eddies, shape of eddies, and area covered by eddies (positive and negative error). For each of the following calculations, the label AE refers to anticyclonic eddies (AEs) while the label CE refers to cyclonic eddies (CEs).

1) NUMBER ERROR

The percentage error between the number of eddies identified by the SSH algorithm (N_{SSH}) and the algorithm to be tested (N_{Test}) was used to eliminate algorithms that over-identify eddies in situations where they should be identifying a fewer eddies and vice versa. It is calculated as:

$$\mathbf{Err_{Num}} = \left|\frac{\mathbf{N_{Test}} - \mathbf{N_{SSH}}}{\mathbf{N_{SSH}}}\right| \tag{8}$$

2) RATIO ERROR

Some eddy detection schemes will frequently falsely classify currents, front, filaments, and other elongated structures as eddies. In order to reduce these false classifications, we can take the ratio of the longest and shortest distances between the eddy edge and the geometric eddy centroid. Therefore, the ratio error is calculated as the percentage error between the average of the ratio in both the SSH algorithm ($Ratio_{SSH}$) and the algorithm to be tested ($Ratio_{Test}$). A ratio closer to 1 reflects a perfectly circular eddy, while a lower ratio reflects an eddy that is either overly elongated or possesses some anomalously extending element such as a filament. This is functionally very similar to the classic circularity test but is much more computationally efficient. We calculate the ratio error as:

$$\mathbf{Err_{Ratio}} = \left|\frac{\mathbf{Ratio_{Test}} - \mathbf{Ratio_{SSH}}}{\mathbf{Ratio_{SSH}}}\right| \tag{9}$$

3) SPATIAL POSITIVE ERROR

This is the percentage error between the area correctly identified as an eddy, either AE or CE, in the SSH algorithm and the algorithm to be tested. This is assessed pixel by pixel using a classification scheme where a pixel labelled 0 is considered to be not an eddy, 1 is considered to be within an AE, and 2 is considered to be within a CE. Any pixels labelled AE or CE are considered to be part of an eddy, or positively detected. This error is calculated as:

$$\mathbf{Err_{Pos}} = \frac{\mathbf{1}}{\mathbf{2}}\left(\left|\frac{\mathbf{FN_{AE}}}{\mathbf{TP_{AE}} + \mathbf{FN_{AE}}}\right| + \left|\frac{\mathbf{FN_{CE}}}{\mathbf{TP_{CE}} + \mathbf{FN_{CE}}}\right|\right) \tag{10}$$

Where TP is the number of true positive pixel identifications, and FN is the number of false negative pixel identifications.

4) SPATIAL NEGATIVE ERROR

This is the percentage error between the area correctly identified as not containing an eddy in the SSH algorithm and the algorithm to be tested, using the same pixel by pixel classification as per the spatial positive error. It is therefore calculated as:

$$\mathbf{Err_{Neg}} = \frac{\mathbf{1}}{\mathbf{2}}\left(\left|\frac{\mathbf{FP_{AE}}}{\mathbf{TN_{AE}} + \mathbf{FP_{AE}}}\right| + \left|\frac{\mathbf{FP_{CE}}}{\mathbf{TN_{CE}} + \mathbf{FP_{CE}}}\right|\right) \tag{11}$$

where TN is the number of true negative pixel identifications with the SSH algorithm considered to be the truth, and FP is the number of false positive pixel identifications.

5) AGGREGATE SIMILARITY SCORE

This is the aggregate score, *S*, used to optimize eddy detection methods. It is calculated using an arithmetic mean of the above errors:

$$\boldsymbol{S} = \left[\mathbf{1} - \frac{\mathbf{1}}{\mathbf{4}}\left(\mathbf{Err_{Num}} + \mathbf{Err_{Ratio}} + \mathbf{Err_{Pos}} + \mathbf{Err_{Neg}}\right)\right] * \mathbf{100} \tag{12}$$

A perfect similarity score of 100 indicates that the test and SSH methods result in the exact same eddy detection scheme with the same number of eddies, in the same shapes, covering all of the same pixels. We therefore attempt to maximize the similarity score of an algorithm in the ensuing analysis, although each individual error is considered in the performance of the results. In our analysis below, there is no weighting given to each of the scores. However, the reader is invited to use arbitrary weighting of the scores in their own applications for their own purposes.

e. Tracking

An eddy tracking methodology is required to verify the identification of specific eddies over multiple time steps. In this study, we use the eddy tracking algorithm developed by Chaigneau et al. (2008) and Pegliasco et al. (2015). This algorithm has since been used in the Arabian Sea to describe the nature and variability of both the eddy field as a whole and to characterize specific climatological eddies (Ernst et al., 2022; Trott et al., 2018). This algorithm compares eddies with overlapping areas between subsequent time steps using a cost function based upon the differences in radii, amplitudes, and EKE of each eddy. A minimum of this cost function represents the most statistically similar and thus likely eddy trajectory to continue

tracking. A comprehensive description of this tracking algorithm can be found in Trott et al. (2018). It is worth noting that any other tracking algorithms may be used in conjunction with our detection scheme.

f. Optimization Domain

All optimizations are performed between 10ºS and 30ºN, 40ºE and 80ºE, and over the winter (November, December, January, February) and summer (May, June, July, August, September) monsoons of 2016, 2017, and 2019 to encompass the Arabian Sea. These years were chosen as their monsoons cover each classification of monsoon from weak (2016) to normal (2017) to strong (2019) and so provide variation of the Arabian Sea eddy field to fully test each parameter (Ernst et al., 2022; Greaser et al., 2020). All eddies with a radius smaller than 25 km are eliminated from our results, as these eddies are below the mesoscale (defined here as smaller than the first baroclinic deformation radius, approximately 50 km in the central Arabian Sea) and currently lack altimetric verification for the SSH method in the Arabian Sea (Le Vu et al., 2018). The total number of eddy maps (days) across all tested monsoons is 837, with the SSH method at the surface finding a total number of 24,681 CEs and 23,532 AEs before individual detections are collated into trajectories.

3. Eddy Tracking Optimization

a. Center Thresholds

To begin our search for an optimized detection method, we separate the center- and edge-finding components and test their parameters separately. First, we optimize the thresholds of the methods that require them, namely $VORT_T$, OW_T, and LNAM. We do this by using the SSH edge component, ensuring that the edge-finding method is the same for each center method tested (Fig. 1).

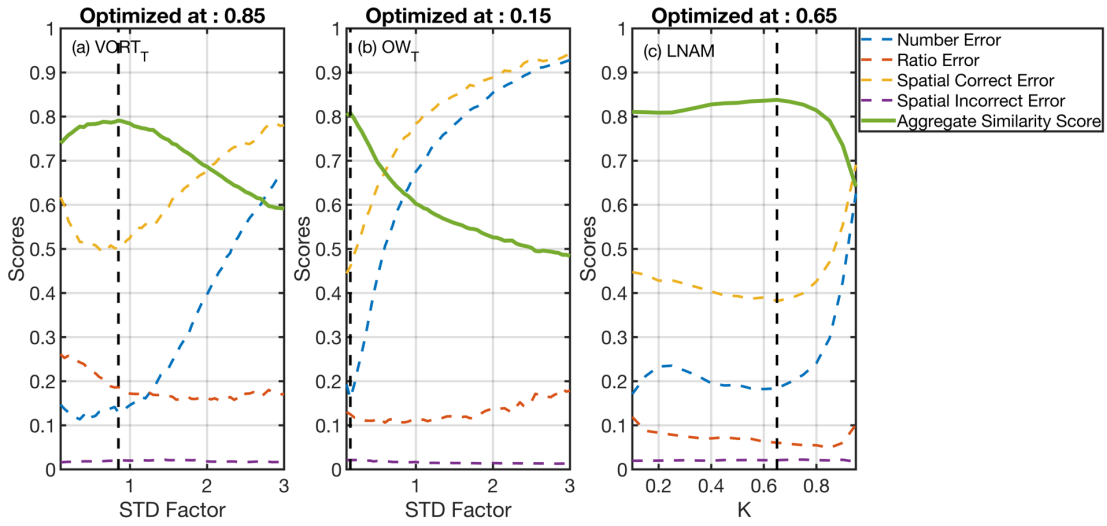

Figure 1. Optimizations of the center threshold parameters of $VORT_T$ (a), OW_T (b), and LNAM (c) with each type of error and score. The STD factor for OW_T is considered to be always negative, as only a negative OW is associated with eddy centers.

We find that the optimized center threshold values of 0.85 for $VORT_T$ (Fig. 1a), 0.15 for OW_T (Fig. 1b), and 0.65 for LNAM (Fig. 1c). We note that the optimum threshold parameter is most heavily determined by the number and the spatial positive errors, with only a slight variation in ratio error and very little change in spatial negative errors. We find that these thresholds lie closely to values found in the literature, *i.e.* 0.2 for OW_T's STD factor and 0.7 for LNAM's K (Isern-Fontanet et al., 2003; Le Vu et al., 2018; Xu et al., 2019). However, our optimal values are smaller by 0.05 in both cases, reflecting a very slightly more lenient threshold. Overall, only OW_T favors a single optimum value based upon its aggregate score, while $VORT_T$ and OW_T each have a wide range of similar values higher than 0.7; $VORT_T$ scores are similar between a STD factor of 0.5 and 1, while LNAM scores have the largest range of comparable values between 0.1 and 0.8, which also matches the findings of Le Vu et al. (2018). All further analysis with these methods is hereafter performed with the optimized values determined above.

b. Center Filtering

Given the high resolution of the model used and the noise often contained within the non-normalized vorticity derived fields, a simple low-pass moving average filter may be applied to the data to enhance detectability of mesoscale features (Souza et al., 2011). The size of this filter, if it should be applied at all, may also be optimized, with the number of pixels on

each side of the center pixel (the half window) denoting the smoothing factor (Fig. 2). In this case, an increase in smoothing factor by 1 increases the size of the low-pass filter by 1/12º on all sides, such that a maximum tested smoothing factor of 15 is a filter of 31 pixels by 31 pixels (including the center pixel), or approximately a 280 km low-pass filter depending on latitude.

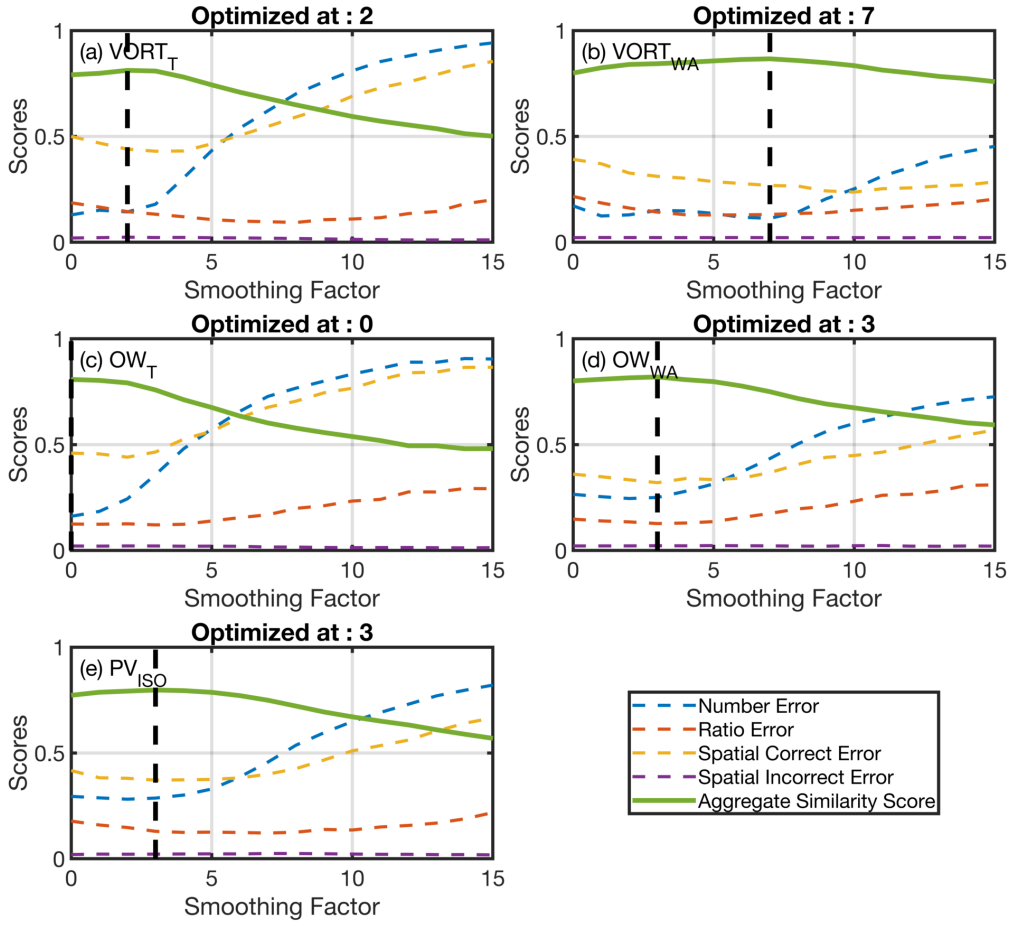

Figure 2. Smoothing factors optimized for the center components of $VORT_T$ (a), $VORT_{WA}$ (b), OW_T (c), OW_{WA} (d), and PV_{ISO} (e) for each type of error and score. STD factors are the optimized values in Fig. 1.

We find that the optimal smoothing factors for each field are 2 for $VORT_T$ (Fig. 2a), 7 for $VORT_{WA}$ (Fig. 2b), 0 (no smoothing) for OW_T (Fig. 2c), 3 for OW_{WA} (Fig. 2d), and 3 for PV_{ISO} (Fig. 2e). Of these optimizations, $VORT_T$ and OW_T are the most sensitive, with higher smoothing factors drastically increasing both number and spatial correct errors. OW_{WA} and PV_{ISO} are only slightly less sensitive, with increasing number and spatial correct errors on either side of the optimized value. Lastly, $VORT_{WA}$ is relatively stable, with little difference between

high and low smoothing factors. As with the threshold values obtained in section 3a, we continue with the optimized smoothing factors above.

c. Edge Thresholds

$VORT_T$ and OW_T can be decomposed into center and edge thresholds which may be considered separately (Fig. 3). For this purpose and for other edge method optimizations, the center method is set to SSH to remain constant.

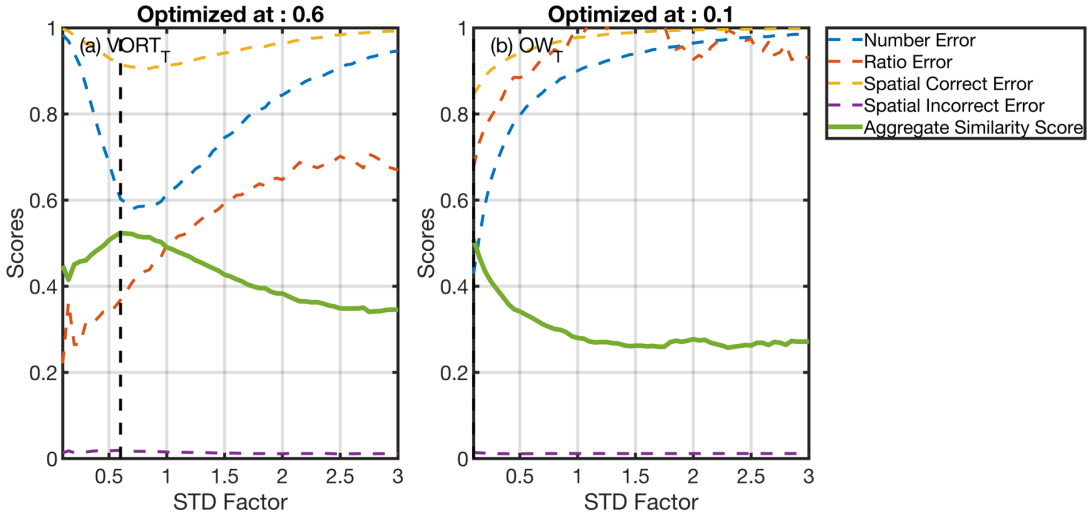

Figure 3. Optimizations of the edge threshold parameters of $VORT_T$ (a) and OW_T (b) with each type of error and score. The STD factor for OW_T is always negative.

We find that $VORT_T$ has an edge STD factor threshold optimized at 0.6 (Fig. 3a) while OW_T is optimized at 0.1 (Fig. 3b). Both STD factors are smaller than their respective center STD factors (Fig. 1), reflecting the need for a more restrictive STD factor to determine the center versus the edge of an eddy. Neither $VORT_T$ nor OW_T compare well to SSH as edge methods, with minimal spatial correct errors of 0.91 and 0.84 respectively, meaning that more than 4 out of every 5 eddy-containing pixels in the SSH method were identified as non-eddies with these methods. This is consistent with previous comparisons that have demonstrated that the OW_T method identifies smaller eddy contours than other methods as compared to the SSH method, which tends to result in relatively large eddy contours (Lian et al., 2019; Souza et al., 2011). We would logically expect that if our 'truth' method were, *e.g.*, a variant of the OW_T method, the spatial positive error would be considerably less for OW_T given the method's resemblance.

d. Edge Filtering and Ratios

As with center methods, we can determine what degree of low-pass filtering might benefit eddy edge detection. We can also filter out elongated fronts and other non-eddy structures using the same axis ratio used for the calculation of the ratio error metric (Section 2, d, 2). In other words, all eddies with a ratio of longest to shortest edge away from the centroid less than a certain threshold are eliminated. In this regard, we vary both the spatial smoothing and minimum ratio together to obtain an optimal result (Fig. 4).

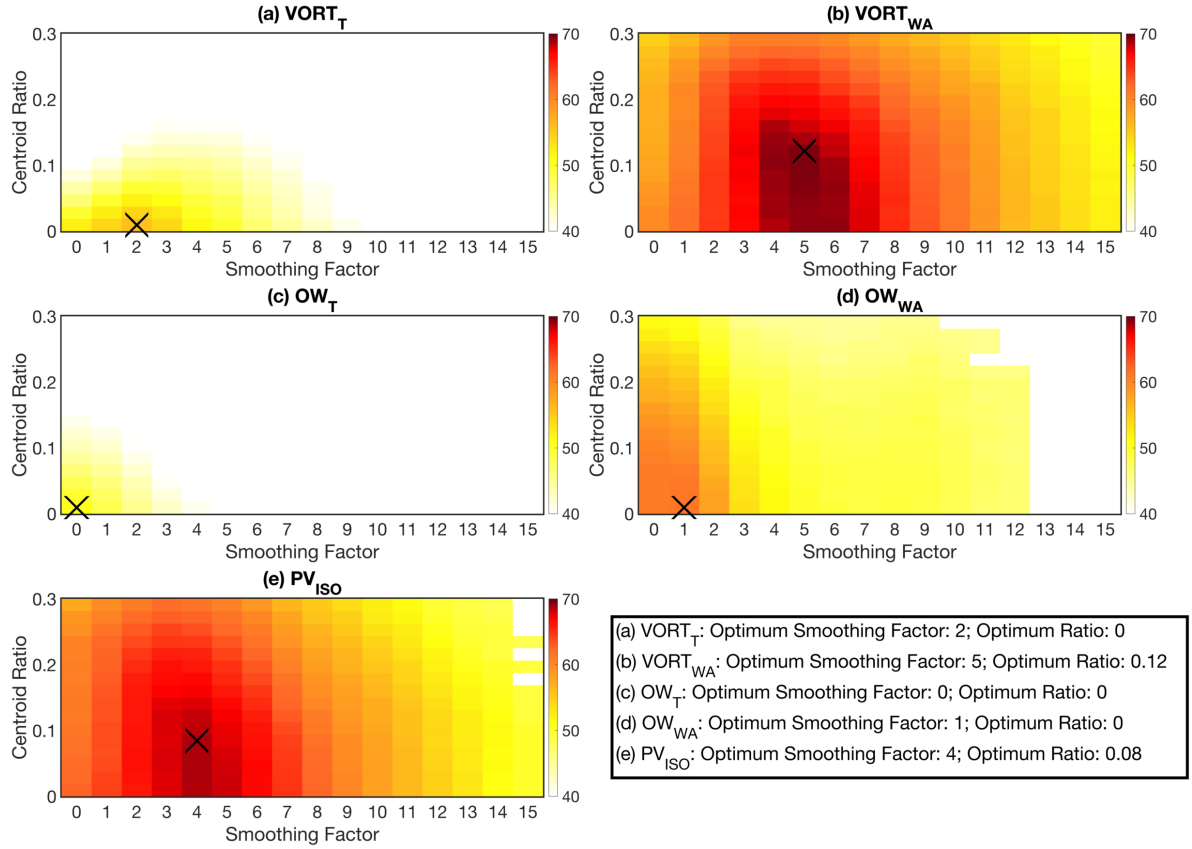

Figure 4. Aggregate similarity score of the edge components of $VORT_T$ (a), $VORT_{WA}$ (b), OW_T (c), OW_{WA} (d), and PV_{ISO} (e) for the optimization of both smoothing factor and minimum centroid ratio using SSH centers. Black Xs mark the combination of smoothing factor and centroid ratio that result in the best similarity score for each edge method tested.

We find that both thresholded methods perform best when relatively unprocessed: $VORT_T$ (Fig. 4a) is optimized at a smoothing factor of 2 with no minimum centroid ratio, while OW_T (Fig 4c) is optimized without smoothing or a minimum ratio. OW_{WA} follows $VORT_T$ in benefiting from a small smoothing factor of 1 and no minimum centroid ratio (Fig. 4d).

$VORT_{WA}$ (Fig. 4b) benefits from moderate smoothing factor of 5 and a minimum ratio of 0.12 and PV_{ISO} (Fig 4e) benefits from a similar smoothing factor of 4 as well as a small minimum centroid ratio of 0.08. We proceed to the final step of method hybridization with these parameters set exactly as in Fig. 4.

e. Hybrid Method Evaluation

Hybrid center and edge detection methods can leverage the strengths of two separate fields or sets of restrictions to produce a superior detection algorithm; AMEDA is one such example, using LNAM for center detection with SSH or geostrophic currents used for edge detection (Le Vu et al., 2018). As a result, we can combine the optimized center and edge methods independently produced by the above analysis to determine if using separate center and edge detection methods creates the optimal hybrid method for subsurface eddy detection when compared to the traditional SSH method (Fig. 5).

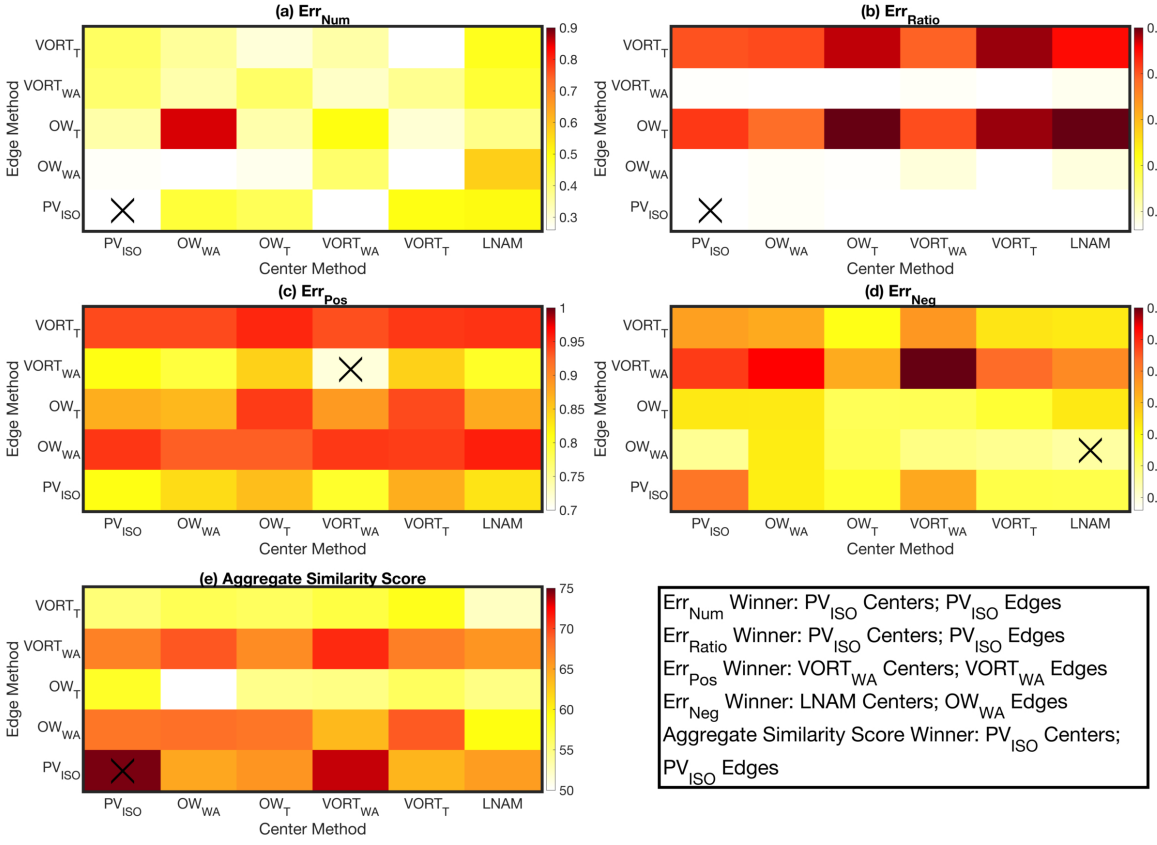

Figure 5. Hybrid method optimization using all center and edge method combinations. Shown are the number error Err_{Num} (a), centroid ratio error Err_{Ratio} (b), spatial correct error Err_{Pos} (c), spatial incorrect error Err_{Neg} (d), and aggregate similarity score (e). Black Xs mark optimal combinations of methods per error and score. Errors are considered optimal when minimized, and similarity score is considered optimal when maximized.

We find that the overall best algorithm is one that utilizes PV_{ISO} for both center and edge detection with a similarity score of 74.65 (Fig. 5e); this algorithm performs best for both number errors (Fig. 5a) and ratio errors (Fig. 5b) as well, with optimal errors of 12.16% and 5.07% respectively. However, both spatial errors have separate optimal algorithms, as Err_{Pos} is optimized with $VORT_{WA}$ centers and $VORT_{WA}$ edges with an error of 71.66% (Fig. 5c) and Err_{Neg} is optimized with LNAM centers and OW_{WA} edges with an error of 1.27% (Fig. 5d). We do note, however, that there is relatively little difference between the best and worst performing Err_{Neg} algorithms versus other error types and that Err_{Pos} is relatively large for all methods, underlining the fact that eddies delimited by SSH have larger contours than any other method. Overall, the best performing edge methods are $VORT_{WA}$ and PV_{ISO} regardless of center methods, while the best overall center method varies by edge method (Fig. 5e). That the winding angle edge algorithms perform better in this analysis is unsurprising, given the winding angle nature of the original SSH algorithm. We would expect that any such comparison would favor similarly constructed algorithms. However, this comparison process is applicable for any original eddy tracking methodology, and so the desirable traits of any other algorithm can be potentially replicated using our overall optimization approach.

Before using any of these hybrid algorithms, we must verify their performance visually to ensure they are detecting eddies sensibly. For this, we select 6 of our algorithms. We first display the SSH algorithm to provide a baseline, then follow with OW_T centers and OW_{WA} edges, as this algorithm is the best performing algorithm using only OW. Then, we demonstrate $VORT_{WA}$ centers and $VORT_{WA}$ edges as the best performing Err_{Pos} algorithm, LNAM centers and OW_{WA} edges as the best performing Err_{Neg} algorithm, $VORT_T$ centers and PV_{ISO} edges as the runner up to the best algorithm, and PV_{ISO} centers and PV_{ISO} edges as the best overall algorithm. We demonstrate each of these algorithms in several times and locations, beginning in the GoA on January 1st, 2017 (Fig. 6).

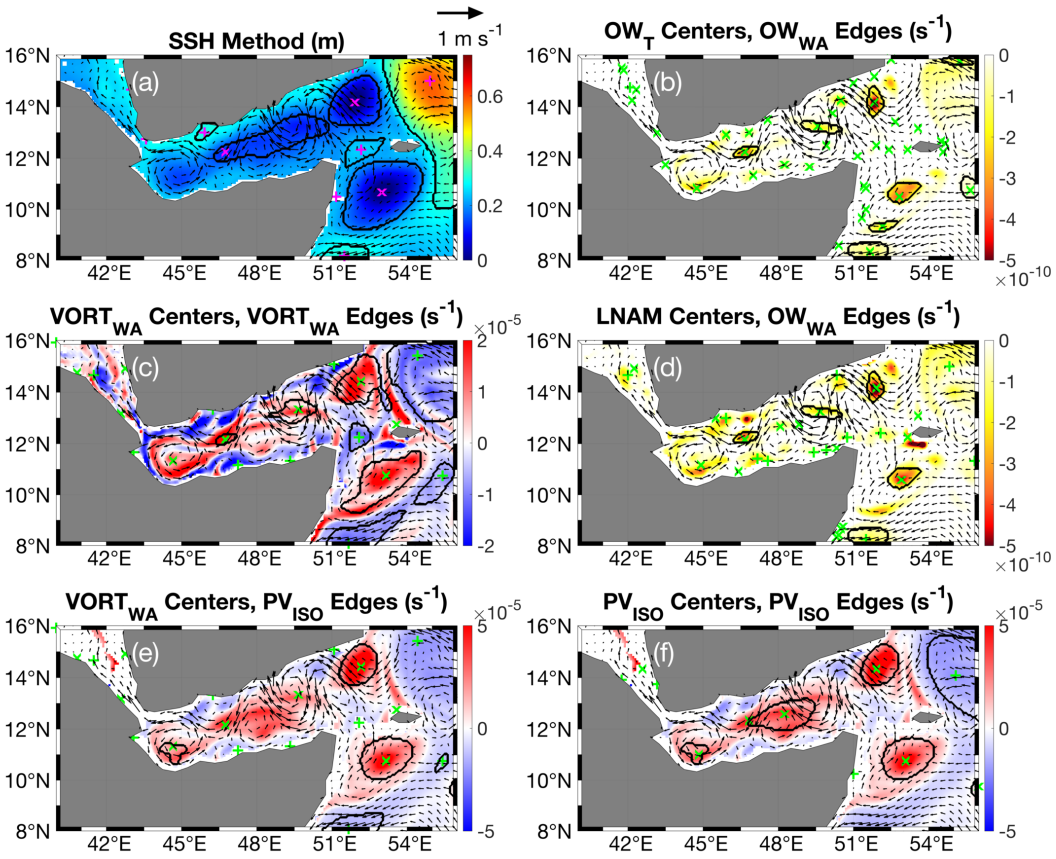

Figure 6. Detected contours (black lines) and centers (+s for AE centers, Xs for CE centers) on January 1st, 2016 in the GoA for the following center/edge hybrid methods: SSH/SSH (a), OW_T/OW_{WA} (b), $VORT_{WA}/VORT_{WA}$ (c), $LNAM/OW_{WA}$ (d), $VORT_{WA}/PV_{ISO}$ (e), and PV_{ISO}/PV_{ISO} (f). Color is given by the edge fields and are shown without low pass filtering. Current vectors are overlaid.

In this snapshot, we find 4 major eddies: an elongated CE in the GoA, two cyclones to the north and south of Socotra, and a large AE partially out of frame to the east (Fig. 6a). All algorithms detect the eddies to the north and south of Socotra, with the PV_{ISO} algorithms achieving the most accurate shapes (Fig. 6e, f). By contrast, only the $VORT_{WA}/VORT_{WA}$ and PV_{ISO}/PV_{ISO} algorithms properly detect the large eastern AE (Figure 6c, f). The middle CE is partially detected in two parts by the OW_{WA} edge algorithms and the $VORT_{WA}/VORT_{WA}$ algorithm, while only the PV_{ISO}/PV_{ISO} algorithm identifies it as a single eddy (Fig. 6b, c, d, f). In terms of smaller eddies, the possible AE to the west of Socotra seen in the SSH method is only identified by the $VORT_{WA}/VORT_{WA}$ algorithm, while the cyclone alone 8ºN is detected by all algorithms except the PV_{ISO}/PV_{ISO} one. Overall, this figure demonstrates that all methods are capable of detecting eddies within the GoA and around Socotra, but that PV_{ISO} algorithms

achieve the most desirable eddy shapes. We continue to see if this is the case using an image of the Gulf of Oman on July 28th, 2017 (Fig. 7).

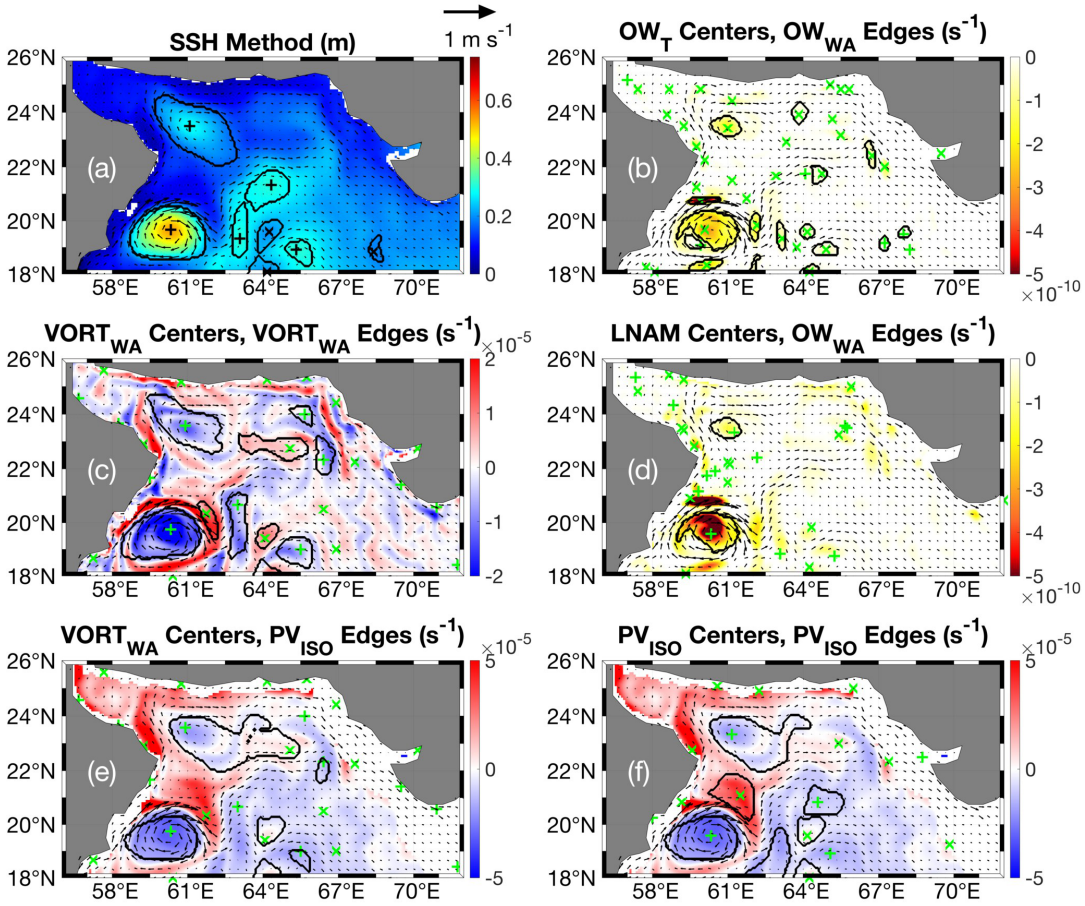

Figure 7. As in Figure 6, but for the Gulf of Oman on July 28th, 2017.

At this point in time, we observe two major eddies in the region, an AE along the southeastern coast of the Arabian Peninsula and exiting the Gulf of Oman (Fig. 7a). These eddies are once again detected by all algorithms, although the PV_{ISO} edge methods additionally identify an elongated section to the east (Fig. 7e; Fig. 7f). Besides these two large eddies, there are a handful of smaller cyclones and anticyclones centered around 64ºE, 20ºN that are partially detected by all methods except LNAM/OW_{WA}. This makes sense, as every other algorithm over-detects smaller eddies in the region, while LNAM/OW_{WA} is optimized for reducing false detections. The OW_T/OW_{WA} and $VORT_{WA}$/$VORT_{WA}$ methods are especially prone to false detections to the northeast. This is reflective of the broader trend of $VORT_{WA}$/$VORT_{WA}$ as seen in Figure 5c and 5d: this algorithm consistently detects almost every eddy in any given image

as it optimizes spatial positive errors, but consistently over-detects, as it has the greatest spatial negative error. This is especially seen in the next series of images of climatological eddies, beginning with the Lakshadweep High (LH) during the northeast monsoon in 2016 (Fig. 8).

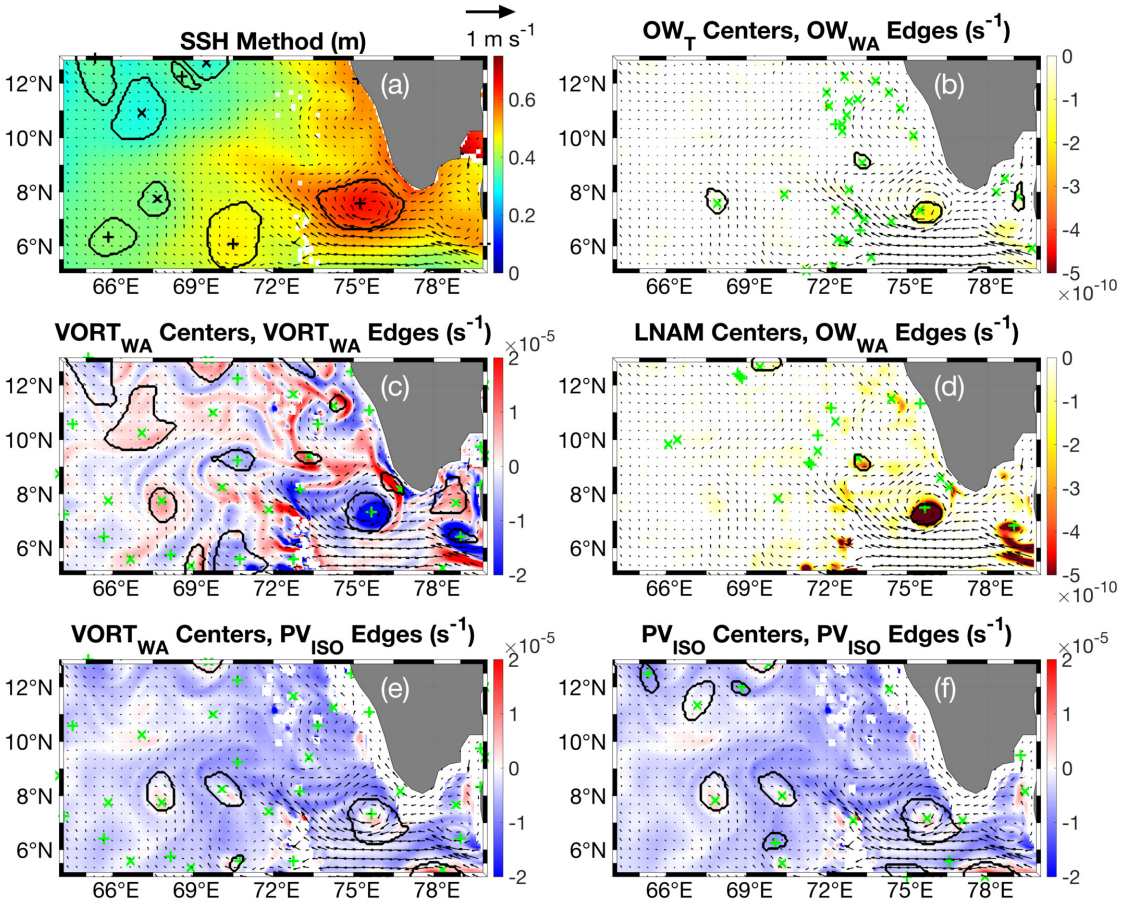

Figure 8. As in Figure 6, but for the Laccadive Sea and West India Coastal Current region on January 1st, 2016.

Here, the LH is centered around 75.8ºE, 7.5ºN, with smattering of less intense AEs and CEs to the west and northwest (Fig. 8a). As before, all algorithms detect the LH, though the PV_{ISO}/PV_{ISO} algorithm makes a curious detection of the LH as an AE, rather than a CE, with a core of positive PV (Fig. 8f). This is only possible due to the isopycnal averaging process detecting a cyclonic core underlying the LH as more powerful than the anticyclonic anomaly at the surface. Misdetections of this manner are not normally the case with this algorithm's performance, but it indicates a reason why its spatial positive error would be higher at the surface, as deeper features can confuse the algorithm. Logically, this would not be an issue in deeper isopycnal layers. Besides the LH, the smaller eddies are best represented by the

PV_{ISO}/PV_{ISO} algorithm, with the other algorithms displaying their common traits as previously highlighted: an over detection of eddies by $VORT_{WA}$/$VORT_{WA}$, an under detection of eddies by LNAM/OW_{WA}, a balanced performance by OW_T/OW_{WA} that tends towards under detection, and a similar performance by $VORT_{WA}$/PV_{ISO} that tends towards over detection (Fig. 8b, c, d, e). To complement this analysis of the LH region and conclude our visual tests, we present a similar snapshot of the Great Whirl (GW) during the strong southwest monsoon of 2019 (Fig. 9).

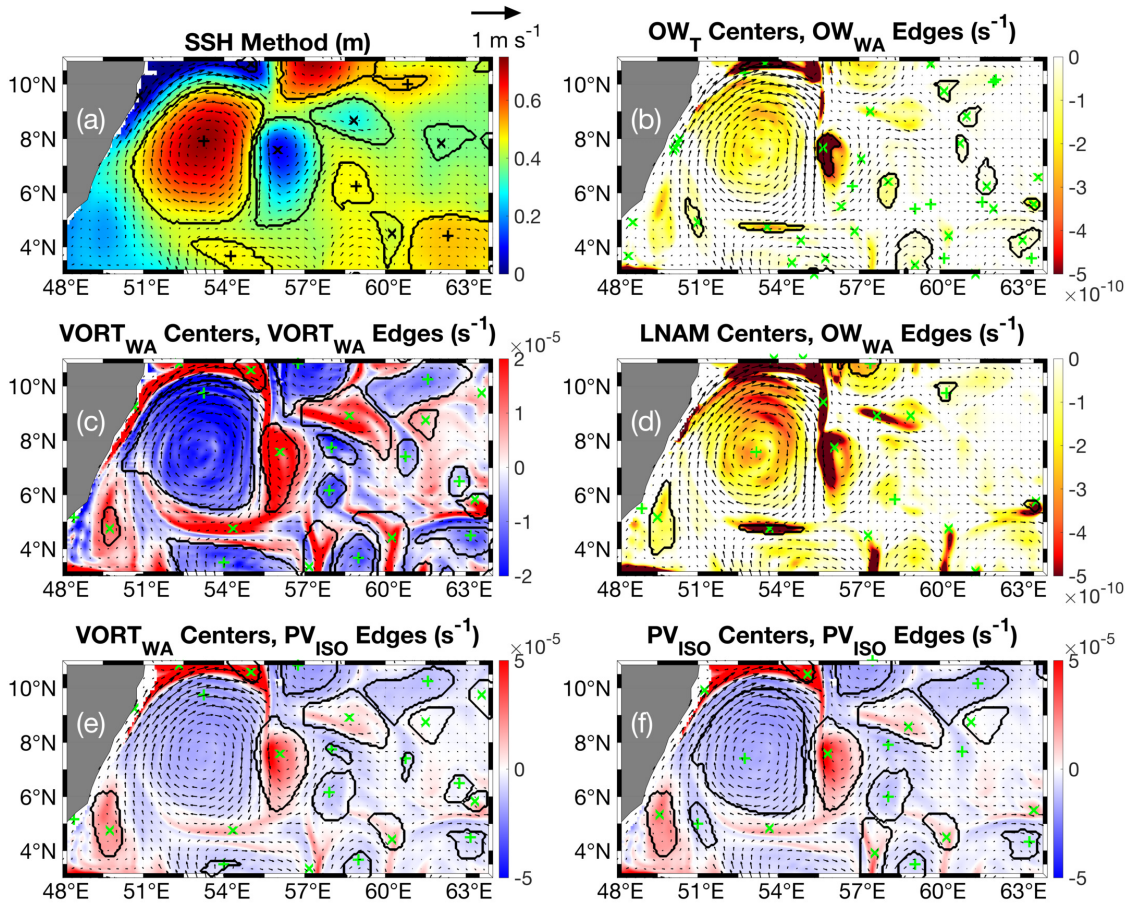

Figure 9. As in Figure 6, but for the Somali Current region on August 28th, 2019.

The GW is evidently the massive AE centered on 53.3ºE, 7.9ºN (Fig. 9a). At this point in time, only $VORT_{WA}$/$VORT_{WA}$ and PV_{ISO}/PV_{ISO} algorithms properly detect it (Fig. 9c; Fig. 9e). By contrast, although centers are identified in every other algorithm, internal variation within the GW prevents a detection. The orbiting cyclone to the GW's east is detected by all algorithms except LNAM/OW_{WA}, a rare failing for this algorithm, while the OW algorithms

521 falsely detect filaments along the southern edge of the GW (Fig. 9b, d). The surrounding
522 energetic eddy field is best represented by PV_{ISO}/PV_{ISO}, although no algorithm perfectly detects
523 every eddy. Every algorithm in this snapshot falsely detects at least one eddy, *e.g.* the possible
524 cyclone to the southwest of the GW that is detected by every algorithm except OW_T/OW_{WA}
525 (Fig. 9b). It is reasonable to conclude that many of these less pronounced detections could be
526 false detections or non-detections by the SSH algorithm. However, as previous studies have
527 concluded, no single algorithm is perfect at detecting all types of eddies, and there is a lack of
528 a unified eddy definition, so our analysis above includes all of the SSH algorithm's features
529 and biases, by nature integrating some of them into our resulting algorithms that emulate it
530 (Lian et al., 2019; Souza et al., 2011).

531 With all of the above analyses considered, we conclude that the best algorithm for use
532 both along isopycnals and in the general sense is PV_{ISO}/PV_{ISO}, specifically with the smoothing
533 factors and centroid ratios we have optimized. By contrast, algorithms that utilize the OW are
534 prone to detecting much smaller eddy contours, often missing eddies entirely and often missing
535 large circulations. Algorithms based around the relative vorticity are functional, but with a
536 tendency to massively over identify eddies.

537 To summarize our final PV_{ISO}/PV_{ISO} optimized method: we first begin with the
538 horizontal velocity fields, temperature, and salinity from our model. We calculate potential
539 density and then rescale the density profile for each vertical column using a representative
540 reference profile defined at a certain location and time (here, 72ºE, 0ºN, recalculated for each
541 monsoon season). This rescaling reduces the effect of the pycnocline on the resultant PV
542 profile. The PV field is averaged between two bounding isopycnals as in Assene et al. (2020).
543 In the figures above, this is done for the surface waters of the Arabian Sea down to 1025.5 kg
544 m^{-3}. This rescaled PV is passed through a simple moving average low pass filter with a half-
545 window of 3 pixels to slightly reduce noise (Fig. 2). Then, we extract local extremes with closed
546 contours of smoothed PV around them and label them as tentative eddy centers. Prior to edge
547 detection, we again smooth the original rescaled PV field in a similar manner with a half-
548 window of 4 pixels (Fig. 3). We then find the largest enclosing contour of PV around each
549 previously identified extreme in the winding angle method style described by previous studies
550 (Chaigneau et al., 2008). Finally, we eliminate all instances of contours with a longest-to-

551 shortest centroid-to-edge distance ratio of less than 0.08, excluding overly elongated, front-like
552 features from the final results (Fig. 3).

553 To summarize, the final optimized parameters for PV_{ISO}/PV_{ISO} and all other algorithms
554 are placed in Table 1.

555

Method	***Optimal Smoothing (Pixels)***	***Optimal Smoothing (Kilometers)***	***Optimal Ratio***	***Optimal Threshold Parameter***	***Optimal Partner Method***	***Final Similarity Score***
$VORT_T$, Center	2	19		0.85 * STD	OW_{WA}	69.18
$VORT_T$, Edge	2	19	0	0.6 * STD	$VORT_T$	58.98
OW_T, Center	0	0		0.15 * STD	OW_{WA}	67.86
OW_T, Edge	0	0	0	0.1 * STD	PV_{ISO}	58.48
$VORT_{WA}$, Center	7	65			PV_{ISO}	73.48
$VORT_{WA}$, Edge	5	46	0.12		$VORT_{WA}$	71.01
OW_{WA}, Center	3	28			$VORT_{WA}$	69.28
OW_{WA}, Edge	1	9	0		$VORT_T$	69.18
LNAM, Center				0.65 (K)	$VORT_{WA}$	65.90
PV_{ISO}, Center	3	28			PV_{ISO}	74.65
PV_{ISO}, Edge	4	37	0.08		PV_{ISO}	74.65

556 *Table 1. The summary of final parameters for all tested detection methods as individually noted*
557 *in Figures 1-5. Kilometer values for optimal smoothing are approximate, rounded values given*
558 *the variation of longitude with latitude and are intended primarily for reference within our*
559 *specified domain.*

560

561

562

4. Case Study: Red Sea Water

a. Isopycnal Evaluation.

In this section, we demonstrate the procedure by which eddies within a water mass can be tracked using our method. We begin with a brief case study of RSW, using our diagnostics to pinpoint a new large eddy identifiable exclusively in the subsurface. However, we must begin this demonstration by defining the RSW domain in our model. Previous studies have determined several isopycnals along which the RSW water mass lies based upon observations (L'Hégaret et al., 2021; Prasad & Ikeda, 2001). Although exact ranges vary depending on the distance from the strait of Bab-el-Mandeb, strict definitions of RSW might choose isopycnals of 1027 kg m^{-3} and 1027.4 kg m^{-3}, while more loose boundaries might define isopycnals of 1026.5 kg m^{-3} and 1028 kg m^{-3}. In order to determine the isopycnals along which we determine the RSW water mass to be for our model, we must validate it against observations. In this case, we use the methodology of L'Hégaret et al., 2021 to determine our isopycnals (Fig. 10).

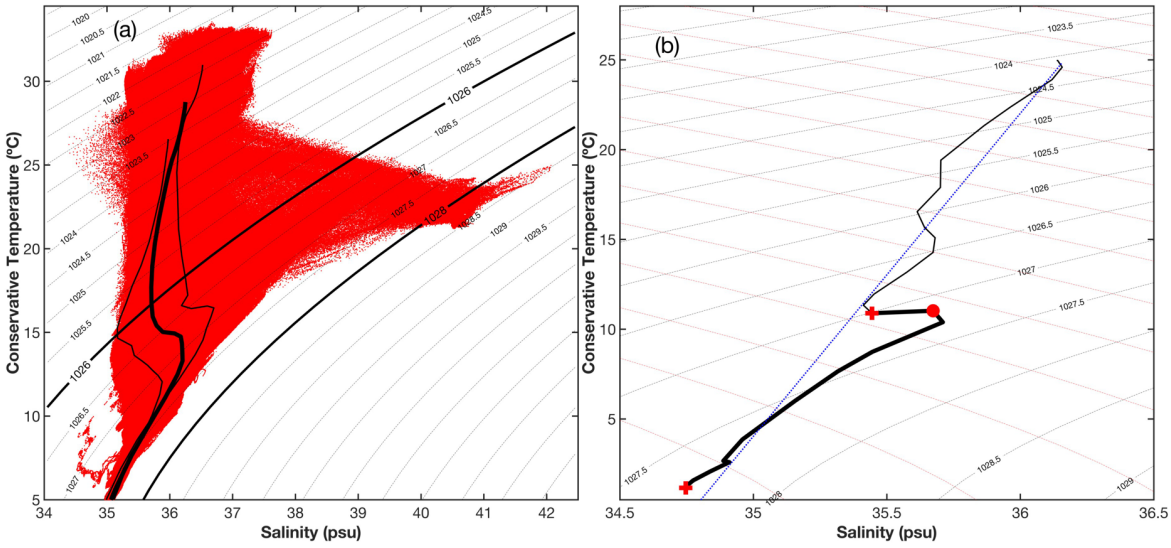

Figure 10. The isopycnal limits of RSW. (a) T-S diagram for the GoA with the median profile ± one standard deviation; the boundary isopycnals (kg m^{-3}) defined by L'Hégaret et al. (2021) are bolded. (b) The L'Hégaret et al. (2021) algorithm for RSW water mass detection on a vertical profile located at 55°E, 13°N on July 7th, 2018. The vertical spiciness trend to be removed is the dotted blue line. The bolded portion of the profile lies between the bolded isopycnals in (a) and below 600 m; the red circle denotes the maximum of the RSW while the red crosses represent the upper and lower minimums.

584 Comparing to L'Hégaret et al. (2021) Figures 3b and 4b, we find that the NEMOv3.1
585 model results in the GoA are on average 0.5 kg m^{-3} less dense at the peak density at depth (Fig.
586 10a) with a much wider spread of salinity values in the intermediate layers. Regardless, the
587 peak of the RSW still is encapsulated broadly by the 1026 kg m^{-3} and 1028 kg m^{-3} bounding
588 isopycnals in the GoA. We use these values to repeat the L'Hégaret et al. (2021) water mass
589 detection algorithm at each vertical profile. First each T-S profile is converted into spiciness
590 following the Gibbs SeaWater (GSW) Oceanographic Toolbox of TEOS-10; this uses the
591 McDougall and Krzysik (2015) formulation of spiciness. Then, the spiciness profiles are
592 vertically detrended, and the previously defined isopycnals, combined with a minimum upper
593 depth of 600 m, are used to define the range of possible depths within which we locate RSW.
594 Within this range of values, a maximum, upper minimum, and lower minimum spiciness are
595 defined (Fig. 10b). We therefore calculate the temporal averages of these values and determine
596 the basin-wide maxima and minima (Fig. 11).

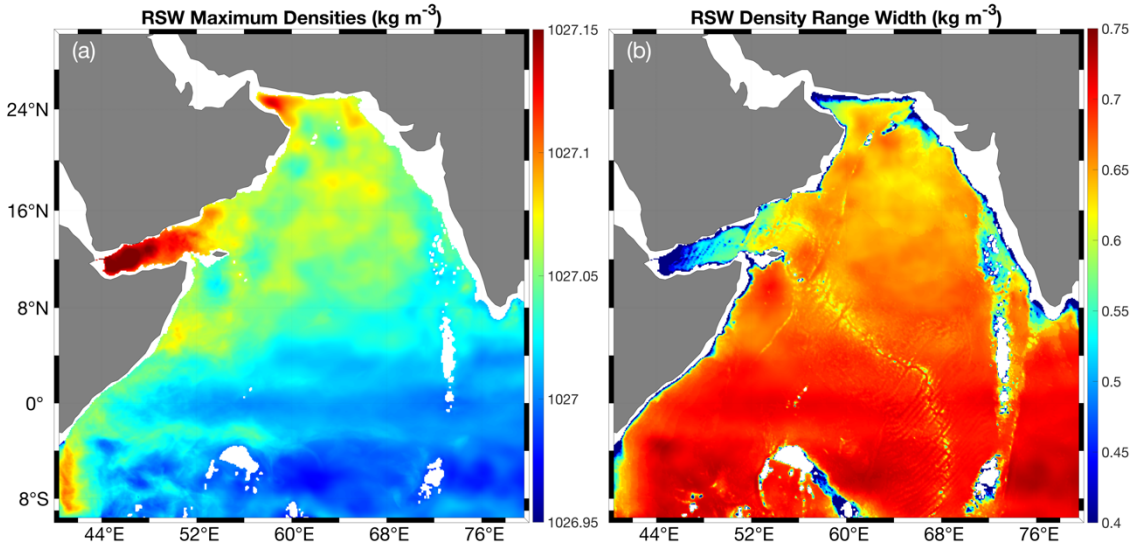

597

598 *Figure 11. (a) The maximum densities (kg m^{-3}) within the RSW isopycnal bounds in our model.*
599 *(b) the range width between the upper minimum and lower minimum bounds of RSW density*
600 *within the isopycnal bounds defined above (kg m^{-3}).*

601 We find that the average RSW maximum decreases away from the strait of Bab-el-
602 Mandeb, scaling from 1027.2 kg m^{-3} at the strait to 1027.1 kg m^{-3} at the edge of the GoA and
603 out to 1027.05 kg m^{-3} in the central and northern Arabian Sea (Fig. 11a). Overall, the vast
604 majority of the RSW maximums (within 2 standard deviations) in our model are found between
605 1026.95 and 1027.3 kg m^{-3}. The opposite trend is seen in the density ranges, as the density

606 ranges are most constrained closer to Bab-el-Mandeb at 0.2 kg m^{-3}, increasing rapidly to the
607 edge of the Gulf and out to 0.6 and 0.7 kg m^{-3} in the northern and southern Arabian Sea
608 respectively (Fig. 11b). We find that the density range width often follows bathymetry, with
609 the shoaling of the Central Indian Ridge clearly visible as a decrease in density range. This
610 reflects the propensity for the bottom minimum to lie literally on the bottom of the bathymetric
611 model mesh throughout this region. The majority of the density range is the difference between
612 the maximum and the bottom minimum, rather than the top minimum; the average difference
613 between the top minimum and the maximum is 0.037 kg m^{-3}, while the difference between the
614 bottom minimum and the maximum averages 0.6 kg m^{-3}. With these numbers in mind, we aim
615 to capture eddy dynamics in the maximum of RSW, constricting our depth range enough that
616 we do not average over too many layers. We therefore choose an isopycnal range between
617 1026.95 kg m^{-3} and 1027.4 kg m^{-3} for the following analysis. This contains all RSW maxima
618 to within 3 standard deviations, with an upper bound adhering to the findings of Prasanna
619 Kumar & Prasad (1999). Across the Arabian Sea in the model domain and time period studied,
620 the average depth of the former isopycnal is 633 m and the average depth of the latter isopycnal
621 is 1034 m, encompassed by NEMO model levels 32 through 36. As our reference profile
622 location typically does not display a major signature of RSW, we maintain its use for our results
623 as described in Section 2f.

624 We will now proceed to provide a brief overview of the results of our methodology.
625 The total results as summarized below are best interpreted using our Movies S1 and S2 that
626 present the PV and Spiciness of the Arabian Sea in conjunction with our detected eddies and
627 their respective tracking numbers over time. We encourage the reader to examine these movies
628 and note that, while many eddies are correctly identified, as noted by the spatial positive error
629 from Fig. 5, our method is not perfect, but can, as demonstrated below, still provide a useful
630 tool for characterizing subsurface eddies that exist within specific water masses.

631 *b. Red Sea Water Eddy Tracking*

632 We find that the largest number of eddies by category are CEs produced in the summer
633 monsoons (Fig. 12i-j), with the largest generation sites at the mouth of the Gulf of Oman and
634 along the Somali Current. By contrast, the winter monsoon CEs are detected most frequently
635 along the West Indian Coastal Current (WICC) (Fig. 12a-b). While the summer monsoon CE

636 distribution is consistent with previous studies of surface eddies, such as Zhan et al. (2020), the
637 winter CE distribution is unanticipated. The most likely explanation is Rossby wave activity
638 radiating from the second annual downwelling coastal Kelvin wave each year, as the westward
639 trajectories and phase speeds of these eddies suggest this origin (Brandt et al., 2002;
640 Subrahmanyam et al., 2009). Additionally, Wang et al. (2021) demonstrate that the signals of
641 baroclinic Rossby waves are visible in the vorticity balance even past 1000 meters, albeit
642 weakly. Another reasonable source of these eddies might be a long-lasting meander in the RSW
643 outflow tongue, as documented observationally by Meschanov & Shapiro (1998). AEs in the
644 winter also are mainly found along the axes of what could be either Rossby waves or the RSW
645 outflow tongue (Fig. 12f). AEs during the summers are more scattered, with a large number of
646 AEs detected around both in the WICC region and around Socotra (Fig. 12 m-n). The
647 prevalence of AEs in the eastern Arabian Sea during the summer is less supported by surface
648 observations and may be assisted due to the deepening of the WICC undercurrent during the
649 summer (Chaudhuri et al., 2021; Trott et al., 2018). If this is the case, then we will expect large
650 levels of interannual variability in this region (as observed by Chaudhuri et al., 2021).

651 Regardless of the season, the largest and most intense eddies are detected in the Somali
652 Current and the GoA (Fig. 12c-d, g-h, k-l, o-p). Intense RSW eddies are expected in the GoA,
653 as RSW both lies along the bottom and encounters waters from the south, subjecting it to
654 mixing and bottom friction simultaneously (Al Saafani & Shenoi, 2007; de Marez et al., 2020).
655 This spreading also corresponds to previous observations of eddies in the RSW, where
656 instabilities in the spreading out of the GoA is indicated as the primary eddy formation
657 mechanism (Shapiro & Meschanov, 1991). This may help explain the relative deficit of eddies
658 directly in the mouth of the GoA versus the proliferation of eddies further east. Unusually,
659 there is a small region where an above-average number of large, very intense Antarctic
660 Intermediate Water (AAIW) eddies are detected around 8ºS, 73ºE. This corresponds to the
661 region around the Chagos Archipelago and has not been documented to this point (Trott et al.,
662 2017; Trott et al., 2019; de Marez et al., 2019).

663

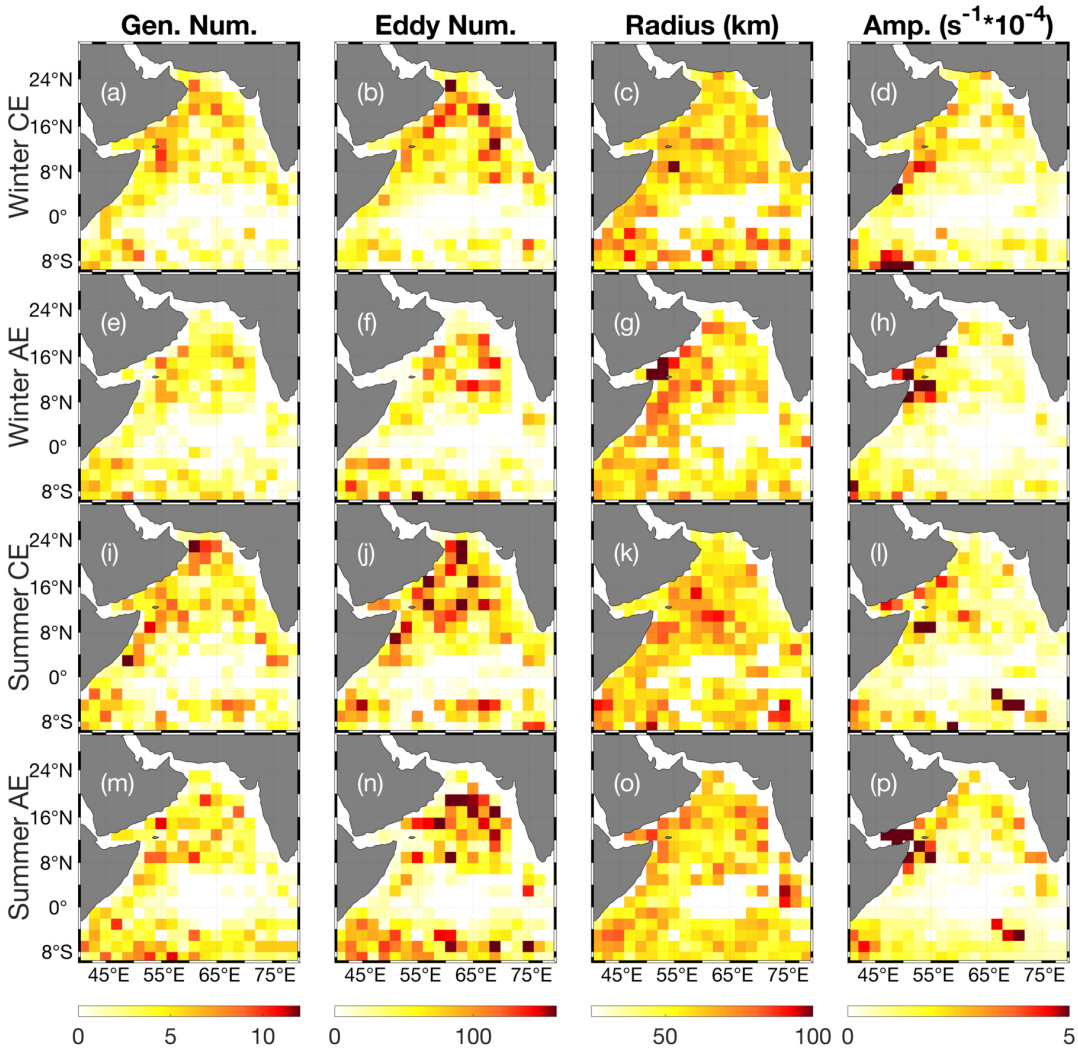

664

665 *Figure 12. The properties of each type of RSW eddy separated by monsoon in 2°x2° bins: Winter*
666 *CEs (a-d), Winter AEs (e-h), Summer CEs (i-l), and Summer AEs (m-p). Gen. Num. refers to*
667 *where eddies are first detected. Radius and Amplitude (absolute value) are average values.*

668 *c. A Chagos Eddy and its Potential Vorticity Evolution.*

669 To demonstrate the dynamical analysis that is more easily enabled with the PV_{ISO}/PV_{ISO}
670 method, we investigate the anomalously intense AEs that form near the Chagos Archipelago
671 as identified in Figure 12, hereafter referred to as the Chagos eddies. These eddies form
672 frequently around the Chagos Archipelago during the southwest monsoon, and select one such
673 eddy on May 29th, 2019 (eddy ID 998 in Movie S1 and Movie S2), which had first been
674 identified 16 days earlier and would continue to remain identifiable as a high PV core until late

July, although our algorithm loses track of it after mid-June due to edge interference with the Chagos Archipelago (Fig. 13).

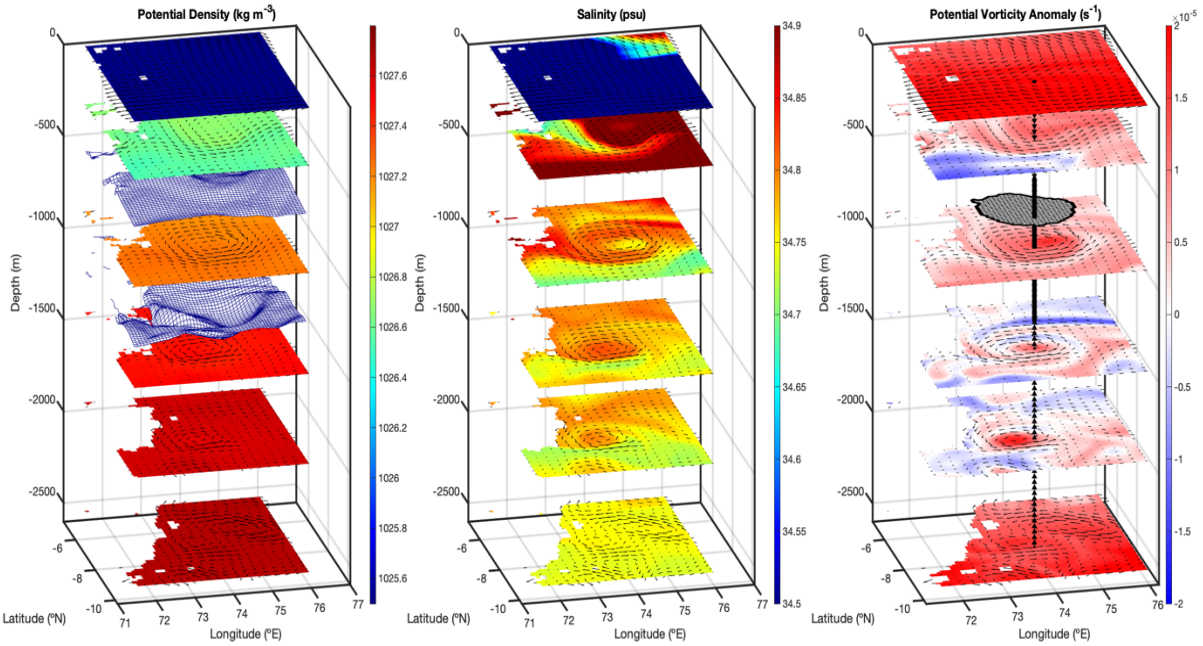

Figure 13. The three dimensional structure of a Chagos eddy on May 29th, 2019 with NEMO levels 2, 29, 35, 38, 40, and 42 displayed. Column 1: the potential density (kg m^{-3}) and current vectors on each level, with mesh grids marking the upper (1026.95 kg m^{-3}) and lower (1027.4 kg m^{-3}) isopycnal bounds within which the eddy is defined in our algorithm. Column 2: the salinity (psu) and current vectors of the column. Column 3: The PV anomaly (s^{-1}) and current vectors of the column with a mesh contour defining the algorithmically defined boundaries of the eddy within the layers of Column 1. A black line marks the center point of the eddy, with a solid line marking the target density layer and spaced triangles marking depths outside of the target density layer.

We observe the deformation of the isopycnals downward in the water column (Fig. 13, Col. 1) between 600 and 1200 meters. This is accompanied by an anticyclonic vortex that is positioned between a high salinity water mass to the north and a low salinity water mass to the south, with a peak salinity at approximately 700 meters' depth (Fig. 13, Col. 2). This is almost the exact depth of the identified eddy (743 meters maximum PV anomaly), which at this time possesses an average radius of 112 km (Fig. 13, Col. 3). As this lies in the southern hemisphere, this counterclockwise circulation is associated with the downwelling of water in the intermediate ocean. Furthermore, there is no sign of an eddy at the surface, indicating that this eddy is fully subsurface with a signature visible down to 2000 meters.

To determine how this eddy may have formed, we perform Lagrangian particle tracking as described by Assene et al. (2020). This takes 500 particles randomly seeded within the eddy radius and vertically within 100 meters of the maximum PV anomaly depth of the eddy core (Fig. 13, Col. 3) in regions with a vorticity greater than 1×10^{-6} s^{-1}. We calculate the particle's position, PV, and Richardson number (Ri) backwards in time to determine an initial position 100 days prior. Since isopycnal PV is conserved adiabatically, the particles that have experienced the largest changes in PV have therefore undergone mixing, friction, or some other diabatic process. We use the same scheme as Assene et al. (2020) to classify particles as high (initial PV greater than 2 standard deviations above final PV), low (initial PV less than 2 standard deviations above final PV), or medium (initial PV within 2 standard deviations of final PV) starting PV particles, where the standard deviations are calculated using all particles' final PV. These are displayed as red crosses, blue triangles, and green diamonds, respectively. We begin by displaying all 500 particles' evolution and general characteristics through time (Fig. 14).

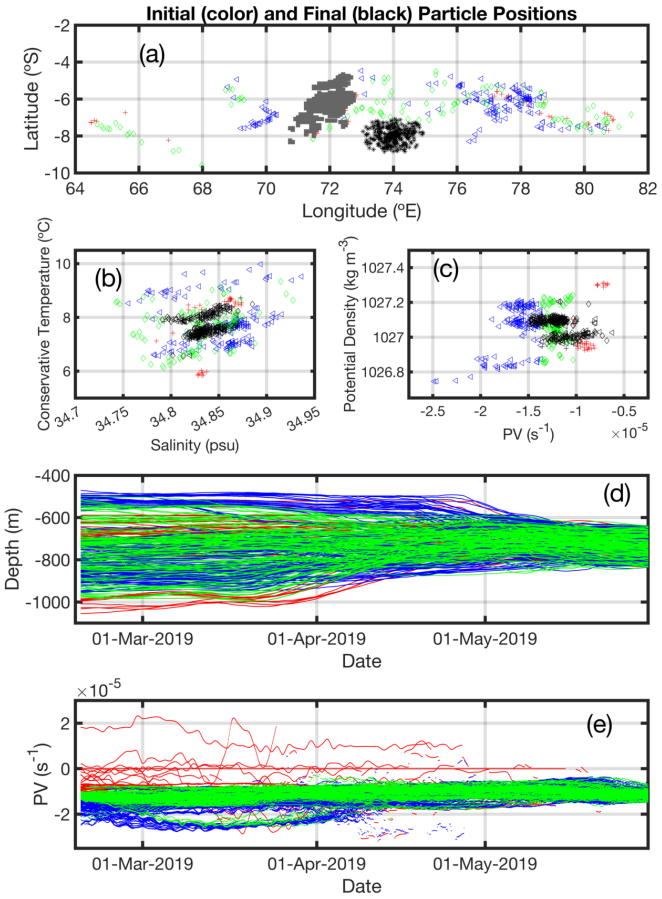

Figure 14. (a) The beginning (February 18th, 2019, colored) and end (May 29th, 2019, black) locations of each type of particle as described in the text (red cross = high PV, blue triangle = low PV, green diamond = medium PV). The Chagos Archipelago is greyed out to the eddy's northwest. (b) A T/S diagram of the initial (colored) and final (black) particles. (c) a density/PV diagram of the initial (colored) and final (black) particles. (d) the depth evolution of each type of particle by date with colors as in (a). (e) as in (d), but with PV.

We find that 56.4%, or 282 of the particles that formed the Chagos eddy were initially low PV, with only 28.6%, or 153 of the particles possessing moderate PV and the remaining 15%, or 75 particles, having high in PV (Fig 14a). 80.6%, or 403 of the particles originate to the east of the Chagos Archipelago, while the remaining 97 particles originate to the west. Low PV particles are the most clustered, found primarily in an eastern grouping centered on 6ºS, 77ºE and a western grouping around 7ºS, 70ºE. By contrast, moderate PV particles are found throughout the entire domain where particles are found, though with the smallest average movement from starting position to ending position, as a large number of moderate PV particles are scattered to the north of the eddy. Finally, the high PV particles are found both in the eastern cluster where the low PV particles are found, as well as the eastern edge of the Chagos Archipelago and the far western edge of the domain around 64.5ºE. The particles' temperatures and salinities display two groupings roughly above and below 7.8ºC, with a notable scattering of low PV particles being the warmest around 9ºC and a tight grouping of high PV particles being the coldest at or below 6ºC (Fig. 14b). As seen by the highly concentrated final positions, particles remain grouped into two halves by temperature, with a range of salinities from 34.8 psu to 34.87 psu. The density groupings in Fig. 14c further make apparent that there are two distinct clusters of density for all particles, regardless of initial PV. The original depths of the particles range from 450 meters to 1100 meters, with low PV particles dominating the layer closer to the surface and high PV particles being the most prevalent in the deepest layer (Fig. 14d). The low PV particles sink by 200 meters around late April, while the high PV particles rise to 900 meters or above by early April. We observe that most particles are clustered around a PV of -1×10^{-5} s^{-1} for most of their lifetime (Fig. 14e). Many of the high PV particles are seen to rapidly vary PV up until the eddy formation in mid-May, while a distinct arc of low PV particles is seen between the end of February and early April; as discussed below, this follows the evolution of another eddy in the region. Overall, PVs are constrained down to their final levels as of early May, just prior to the eddy formation.

First, we consider the evolution of the low PV particles specifically (Fig. 15). We find that there are 226 low PV particles originating to the east of the Chagos Archipelago, and 56 particles originating to the west. The eastern particles mostly originate in the deeper layers around 1027.15 kg m^{-3} (Fig. 15a, b). These are seen to rotate anticyclonically inside another subsurface eddy centered around 8ºS, 77.5ºE before losing PV and mixing with less dense water as they are entrained within the identified Chagos eddy. In fact, this is the result of eddy number 995 in Movie S1 merging with a core of low PV water that is not identified as an eddy until eddy 995 merges with it. This merger is clearly visible in the low Ri numbers around early May, as the two main circulations that eventually become the Chagos eddy merge and mix together. Interestingly, strong PV variations are also associated with low Ri (Fig. 15b, c) and occur at the same time of both the eddies merging and when the resulting structure interacts with the Chagos Archipelago. We observe another anticyclonic subsurface eddy originate in late February around 69ºE to the west of the Archipelago (Fig 19d). In contrast to the eastern eddy, this western eddy is primarily composed of less dense water around 1026.8 kg m^{-3} (Fig. 15e). This eddy impacts the Archipelago as it translates eastward, forcing its particles through a narrow channel that causes substantial mixing and a rapid increase in PV as the particles are forced along the southeastern edge of the Archipelago before finally being entrained in the Chagos eddy late in their lifetime. This mixing is clearly visible in the span of low Ri numbers throughout all of April (Fig. 15f). Overall, the particles that make up the western eddy are the same low PV particles that are warmest and shallowest in Fig. 14.

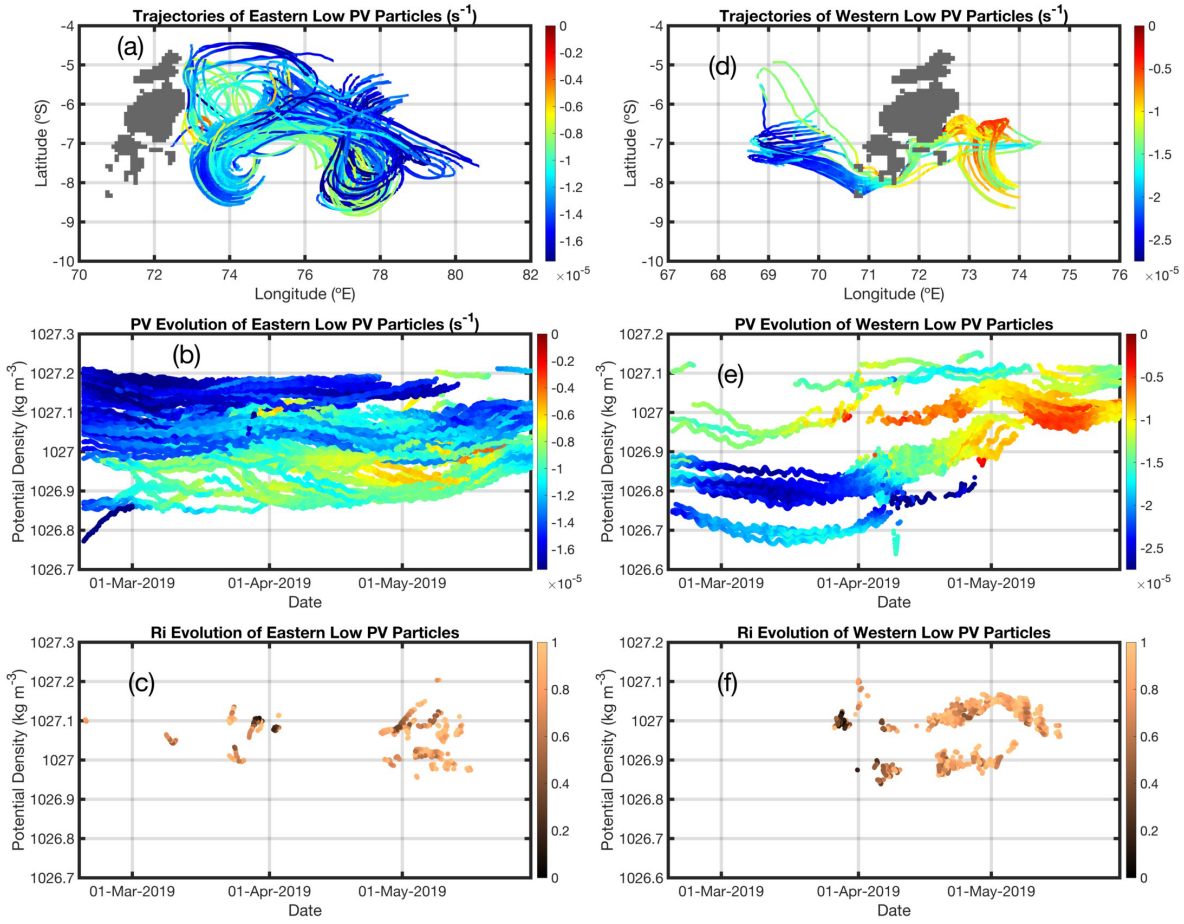

765

766 *Figure 15. The trajectories of eastern low PV particles, colored by PV anomaly (a), the density*
767 *evolution of eastern low PV particles by date (b), and the Richardson numbers below 1 over*
768 *time for eastern high PV particles (c). (d), (e), and (f) are as in (a), (b), and (c) but for western*
769 *high PV particles*.

770

771 We continue our analysis of the different types of particles with the particles that exhibit
772 only a medium PV (Fig. 16). As with low PV particles, the majority (112 of 143) of medium
773 PV particles are found to the east of the Archipelago, with only 31 particles found to the west
774 (Fig. 16a). While around half of the eastern medium PV particles are found to be in the same
775 eddy as identified in Fig. 15 or from a westward current to its east, the other half originate from
776 the north of the final eddy, and are mostly the particles that form the core of the Chagos eddy
777 before it is fully identified as an eddy. This explains their moderate changes in PV and density,
778 as well as only a small amount of mixing around the beginning of May (Fig. 16b, c, d). By

contrast, only 4 of the western medium PV particles follow the same path as the western low PV particles. The remaining 27 particles are advected outside of eddies along an eastward current that is eventually forced along the southern edge of the Archipelago (Fig. 16d). These end up primarily on the southern extreme edge of the Chagos eddy, a delineation made clear from Figure 13, Column 2 as a fresher edge to the south of the eddy. These particles, advected and trapped along the edge of the eddy, most likely do not experience large amounts of mixing, with the exception of one particle in mid-May that experiences a rapid change in PV and density over the course of 3 days (Fig. 16f).

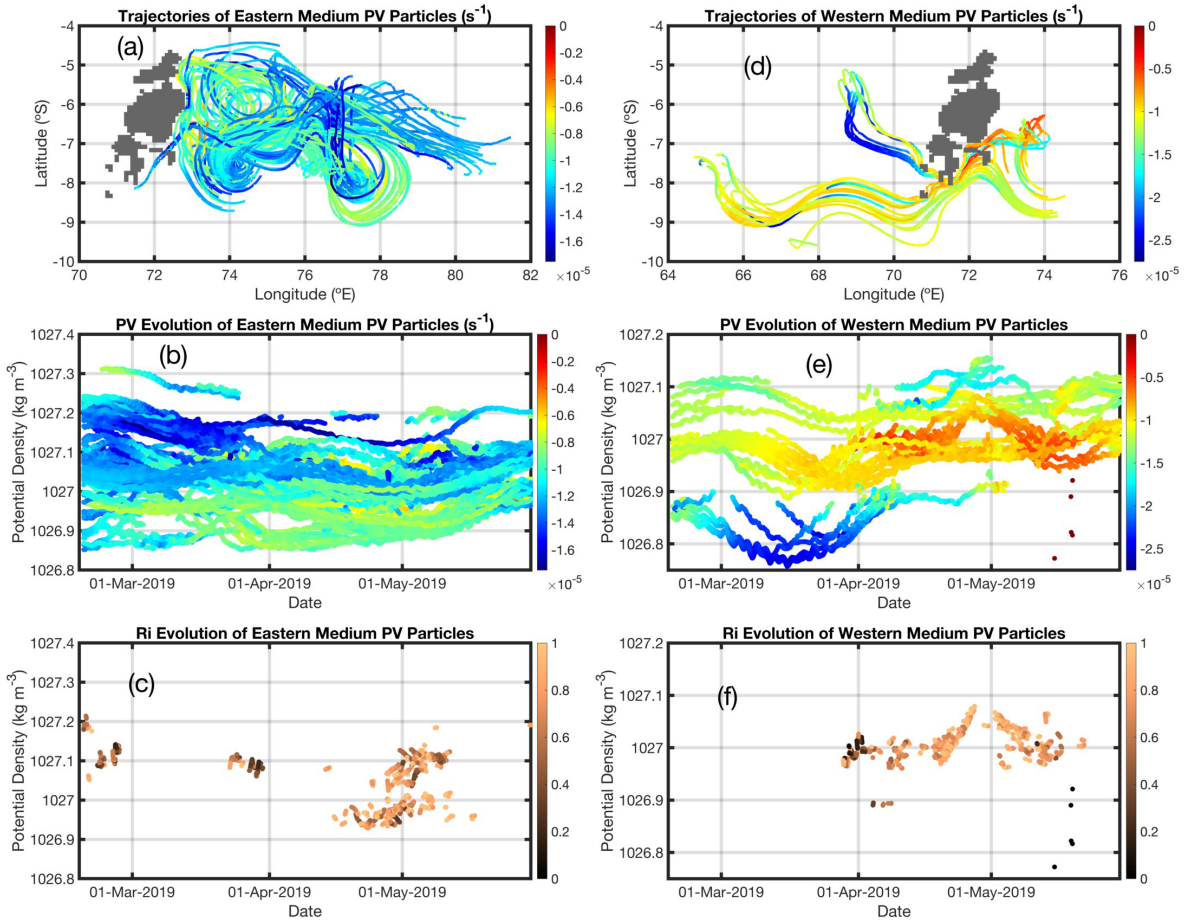

Figure 16. As in Figure 15, but for medium PV particles.

We conclude this analysis with an examination of the high PV particles (Fig. 17). The high PV particles lie almost exclusively to the east of the Archipelago, with 70 of 75 particles found eastward (Fig. 17a). Of the only 5 particles to originate from the west, every single one of them is found as a part of the eastward current identified previously from the medium PV particles in Fig. 16, and so provide no new information (Fig. 17d, e, f). By contrast, the high PV particles to the east of the Archipelago fall into three categories. First, there is a smooth procession of particles with a density of 1026.95 kg m^{-3} from the far eastern edge of the domain that are eventually entrained within the Chagos eddy. These particles only gain PV as they enter the vortex at the end of May. The second group of particles is the same eastern merging AE identified previously; several dense, high PV particles are entrained in this vortex to dramatic effect in early April (Fig. 17b). Finally, there is a grouping of particles that originate from the eastern coast of the Archipelago, many of which start with high PV but almost immediately spike to a PV of nearly -2.5×10^{-5} s^{-1} before eventually joining the low PV particles advected along the edge of the Archipelago and falling in PV around early May. It is these particles that exhibited the most startling changes in PV in Fig. 14e, as they are constantly experiencing friction with the bottom topography in this region until they are advected out of it (Fig. 17c).

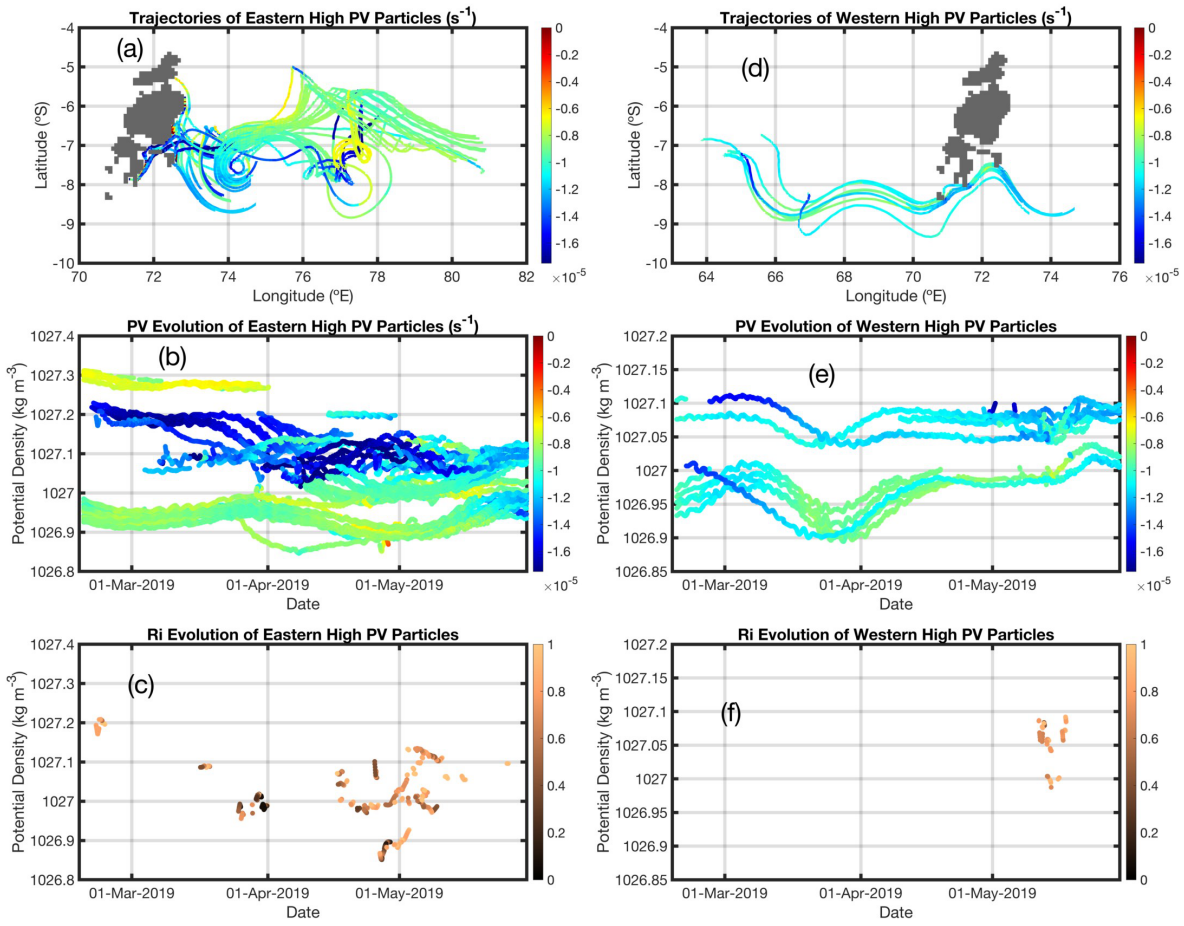

808

809 *Figure 17. As in Figure 15, but for high PV particles defined in Figure 14.*

810 We combine our diagnostics above to provide a qualitative explanation of the likely
811 processes that bring a Chagos eddy on the eastward side of the archipelago into being. First, in
812 each southwest monsoon, the monsoonal winds and the Findlater Jet create the Somali Current
813 and Southwest Monsoon Current (SMC), providing a strong eastward flow along the Equator
814 and to its south (Schott & McCreary, 2001). At around 76ºE, as seen in Schott & McCreary
815 (2001), Fig. 10, this flow encounters a westward current and bifurcates to the north and south.
816 Part of this southern flow then bifurcates again to east and west, resulting in a clockwise loop
817 around the Chagos Archipelago. When the currents to the northeast of the archipelago meet in
818 the wake of the Central Indian Ridge, they are seen to create anticyclonic eddies that then may
819 follow the westward branch back towards the archipelago. At the same time, subsurface eddies
820 and a deep current from the west encounter the geometry of the archipelago and are deflected

northeastwards along its southern edge. Finally, as these eddies converge, they encounter the shallowing of the bathymetry, bringing them to the same depth. As a result, as seen in Fig. 13, Column 2, there is a high salinity, warmer water mass from the north impacting a lower salinity, cooler water mass to the south: given the density surfaces that they lie upon and previous models of water mass mixing in Indian Ocean, we hypothesize that this is diluted RSW impacting AAIW and mixing and being downwelled further into the subsurface intermediate layer (Schott & McCreary, 2001; You, 1998).

5. Conclusions

In this study, we have demonstrated the feasibility of a novel optimization scheme for the development of subsurface eddy detection algorithms against existing surface tracking algorithms, in our case the widely-used winding angle SSH algorithm. We then present the favorable performance of the first eddy detection algorithm exclusively using the rescaled PV averaged across isopycnal layers in an operational forecast model. This detection scheme is tested using the RSW mass in the Arabian Sea and compared against surface and observational studies. We conclude with a Lagrangian analysis of an as of yet undescribed, completely subsurface, intense eddy that forms frequently around the Chagos Archipelago during the southwest monsoon. Through this analysis, we characterize its three dimensional structure, the water masses that form it, and the origin of the particles that comprise it, finding that a combination of instability driven mixing and bottom friction is most likely responsible for the merging of diluted RSW and AAIW. Ultimately, we establish our optimization procedure and resulting rescaled PV algorithm as a new methodology that automatically identifies eddies in isopycnal layers whose dynamics may be efficiently analyzed through further PV diagnostics. Future studies may expand upon our results, using different score weightings, initial comparison algorithms, other tracking algorithms, and other water masses to develop their own version of our method that is optimal for their region of the globe.

Lastly, we would also like to acknowledge a few limitations of and questions raised by our results. Our chosen dataset contains data assimilation, which, when modifying the model fields, acts as a non-conservative process. The temporal continuity of the mesoscale circulation (vortex existence, position, shape and strength) can thus be spoiled. For the CMEMS fields used here, data assimilation is limited and, as shown by the process studies we presented, does not seem to be a strong problem. The approach proposed here presents an opportunity for a

follow up study on the influence of data assimilation in terms of continuity of the PV dynamics and eddy detection algorithms.

Furthermore, our choices of isopycnal bounds for both the surface layer and for the RSW can, as remarked in Section 4a, be slightly altered and still be said to fit their respective water masses. While we have carefully chosen our bounds to align with certain previous observations, our results would change in both quantitative and physically descriptive senses if we aligned our bounds with other descriptions of the layer. Although both the surface layer and RSW layer that we describe are relatively sharply defined (*i.e.* Fig. 10), such sensitivity to choice of bounds might need to be carefully evaluated for water masses with less distinct edges.

Finally, our definition of subsurface eddies is one in terms of PV and renders visible eddies that might be normally difficult to detect through existing methods. However, due to this definition and the paucity of both suitable observational data and previous studies that examine subsurface eddies through this lens, we acknowledge that some of our results as demonstrated above currently lack validation. Indeed, while subsurface dynamics are more conservative than those at the surface due to fluxes across of the ocean-atmosphere interface, implying that our detected eddies at depth might be more physically consistent than those made at the surface, our detections may still yet be improved through a comparison to extensive manual detections in models or detections from appropriate observations in the relevant regions. Regardless, our results above demonstrate the current utility of our method as presented in this work. Given the public repository linked in the Data Availability Statement below, we hope that other researchers will continue to improve upon the foundation we have developed here.

Acknowledgments.

The authors acknowledge no conflicts of interest, financial or otherwise, with respect to the results of this study. This work is supported by ONR Award# N00014-20-1-2742 awarded to BS. PE is funded by the U.S. Department of Defense Science, Mathematics, And Research for Transformation (SMART) Scholarship and the University of South Carolina Presidential Fellowship. This has NRL contribution number JA-7320-22-5656. Approved for public release, distribution is unlimited.

Data Availability Statement.

NEMOv3.1 data is available online at https://resources.marine.copernicus.eu/ courtesy of CMEMS. Strong, weak, and normal monsoon delineation data were obtained from the Indian Institute of Tropical Meteorology at https://www.tropmet.res.in/~kolli/MOL/Monsoon/Historical/air.html. The codebase that comprises the optimization, eddy detection, eddy tracking, water mass tracking, and particle tracking scripts utilized in this work can be found at https://github.com/ErnstPaul/PV-EDDIES-JTECH.

APPENDIX

Calculation of Averaged PV in the Surface Layer

As explained above (see Morel et al, 2019), the generalized PV is closely linked to the quasigeostrophic PV and its vertical integration in a layer bounded by two isopycnals ρ1 and ρ2 is representative of the average dynamics (vorticity and velocity fields). In this case, the mean –generalized- PV representative of the dynamics is given by

$$\overline{\mathrm{PV}}_{\mathrm{rescaled}} = \frac{1}{h_{\rho 1}^{\rho 2}} \int_{z\rho 1}^{z\rho 2} \mathrm{PV}_{\mathrm{rescaled}}\, \mathrm{dz}$$

where $\boldsymbol{h_{\rho 1}^{\rho 2}}$ is the layer depth and $\mathbf{PV_{rescaled}}$ is given by equation (6).

The sea surface is a material surface in adiabatic conditions, but it is generally not an isopycnic surface. However, previous studies have shown that the vertical average of PV is still representative of the dynamics in the surface layer (that is a layer bounded by the sea surface at the top and a chosen isopycnic surface at depth), provided an additional term, associated with density variations at the surface, is added. Indeed, density variation along the surface is equivalent to a Dirac delta sheet of PV that is to be taken into account. Following Schneider et al (2003) and Morel et al (2019) it can be shown that in this case the proper calculation for the equivalent integrated rescaled PV is

$$\overline{\mathrm{PV}}_{\mathrm{rescaled}} = \frac{1}{h_{\rho 1}^{\rho 2}} \left[\int_{z\rho 1}^{z=0} \mathrm{PV}_{\mathrm{rescaled}}\, \mathrm{dz} - (\nabla \times U_{z=0} + f)\, Z(\rho_{z=0}) \right]$$

Where the additional term is calculated from velocity and density fields at the surface (z=0). We also recall that $Z(\rho)$ is the depth at density ρ but associated with a reference profile, representative of the fluid at rest.

This additional term has been proven to be very important for the understanding of the dynamics. Initially Bretherton (1966) discussed it for quasigeostrophic dynamics, which has led to the development of the surface quasigeostrophic theory and models (see Lapeyre et al, 2006 and references therein). Schneider et al (2003) extended the concept to the general case.

REFERENCES

Al Saafani, M. A., and S. S. C. Shenoi, 2007: Water masses in the Gulf of Aden. *J Oceanogr*, **63**, 1–14, https://doi.org/10.1007/s10872-007-0001-1.

Assassi, C., and Coauthors, 2016: An Index to Distinguish Surface- and Subsurface-Intensified Vortices from Surface Observations. *Journal of Physical Oceanography*, **46**, 2529–2552, https://doi.org/10.1175/JPO-D-15-0122.1.

Assene, F., and Coauthors, 2020: From Mixing to the Large Scale Circulation: How the Inverse Cascade Is Involved in the Formation of the Subsurface Currents in the Gulf of Guinea. *Fluids*, **5**, 147, https://doi.org/10.3390/fluids5030147.

Beal, L. M., and K. A. Donohue, 2013: The Great Whirl: Observations of its seasonal development and interannual variability. *Journal of Geophysical Research: Oceans*, **118**, 1–13, https://doi.org/10.1029/2012JC008198.

Brandt, P., L. Stramma, F. Schott, J. Fischer, M. Dengler, and D. Quadfasel, 2002: Annual Rossby waves in the Arabian Sea from TOPEX/POSEIDON altimeter and in situ data. *Deep Sea Research Part II: Topical Studies in Oceanography*, **49**, 1197–1210, https://doi.org/10.1016/S0967-0645(01)00166-7.

Bretherton, F. P., 1966: Critical layer instability in baroclinic flows. *Quarterly Journal of the Royal Meteorological Society*, **92**, 325–334, https://doi.org/10.1002/qj.49709239302.

Chaigneau, A., A. Gizolme, and C. Grados, 2008: Mesoscale eddies off Peru in altimeter records: Identification algorithms and eddy spatio-temporal patterns. *Progress in Oceanography*, **79**, 106–119, https://doi.org/10.1016/j.pocean.2008.10.013.

Chaudhuri, A., P. Amol, D. Shankar, S. Mukhopadhyay, S. G. Aparna, V. Fernando, and A. Kankonkar, 2021: Observed variability of the West India Coastal Current on the

942 continental shelf from 2010–2017. *J Earth Syst Sci*, **130**, 77,
943 https://doi.org/10.1007/s12040-021-01603-4.
944 Chelton, D. B., R. A. deSzoeke, M. G. Schlax, K. E. Naggar, and N. Siwertz, 1998:
945 Geographical Variability of the First Baroclinic Rossby Radius of Deformation. *Journal*
946 *of Physical Oceanography*, **28**, 433–460, https://doi.org/10.1175/1520-
947 0485(1998)028<0433:GVOTFB>2.0.CO;2.
948 ——, M. G. Schlax, and R. M. Samelson, 2011a: Global observations of nonlinear mesoscale
949 eddies. *Progress in Oceanography*, **91**, 167–216,
950 https://doi.org/10.1016/j.pocean.2011.01.002.
951 ——, ——, and ——, 2011b: Global observations of nonlinear mesoscale eddies. *Progress*
952 *in Oceanography*, **91**, 167–216, https://doi.org/10.1016/j.pocean.2011.01.002.
953 Doglioli, A. M., B. Blanke, S. Speich, and G. Lapeyre, 2007: Tracking coherent structures in
954 a regional ocean model with wavelet analysis: Application to Cape Basin eddies.
955 *Journal of Geophysical Research: Oceans*, **112**, https://doi.org/10.1029/2006JC003952.
956 El Aouni, A., 2021: A hybrid identification and tracking of Lagrangian mesoscale eddies.
957 *Physics of Fluids*, **33**, 036604, https://doi.org/10.1063/5.0038761.
958 Ernst, P. A., B. Subrahmanyam, and C. B. Trott, 2022: Lakshadweep High Propagation and
959 Impacts on the Somali Current and Eddies During the Southwest Monsoon. *Journal of*
960 *Geophysical Research: Oceans*, **127**, e2021JC018089,
961 https://doi.org/10.1029/2021JC018089.
962 Fine, R. A., 1993: Circulation of Antarctic intermediate water in the South Indian Ocean.
963 *Deep Sea Research Part I: Oceanographic Research Papers*, **40**, 2021–2042,
964 https://doi.org/10.1016/0967-0637(93)90043-3.
965 Greaser, S. R., B. Subrahmanyam, C. B. Trott, and H. L. Roman-Stork, 2020: Interactions
966 Between Mesoscale Eddies and Synoptic Oscillations in the Bay of Bengal During the
967 Strong Monsoon of 2019. *Journal of Geophysical Research: Oceans*, **125**,
968 e2020JC016772, https://doi.org/10.1029/2020JC016772.
969 Haller, G., A. Hadjighasem, M. Farazmand, and F. Huhn, 2016: Defining coherent vortices
970 objectively from the vorticity. *Journal of Fluid Mechanics*, **795**, 136–173,
971 https://doi.org/10.1017/jfm.2016.151.

Henson, S. A., and A. C. Thomas, 2008: A census of oceanic anticyclonic eddies in the Gulf of Alaska. *Deep Sea Research Part I: Oceanographic Research Papers*, **55**, 163–176, https://doi.org/10.1016/j.dsr.2007.11.005.

Isern-Fontanet, J., E. García-Ladona, and J. Font, 2003: Identification of Marine Eddies from Altimetric Maps. *Journal of Atmospheric and Oceanic Technology*, **20**, 772–778, https://doi.org/10.1175/1520-0426(2003)20<772:IOMEFA>2.0.CO;2.

Lapeyre, G., and P. Klein, 2006: Dynamics of the Upper Oceanic Layers in Terms of Surface Quasigeostrophy Theory. *Journal of Physical Oceanography*, **36**, 165–176, https://doi.org/10.1175/JPO2840.1.

Le Vu, B., A. Stegner, and T. Arsouze, 2018: Angular Momentum Eddy Detection and Tracking Algorithm (AMEDA) and Its Application to Coastal Eddy Formation. *Journal of Atmospheric and Oceanic Technology*, **35**, 739–762, https://doi.org/10.1175/JTECH-D-17-0010.1.

L'Hégaret, P., R. Duarte, X. Carton, C. Vic, D. Ciani, R. Baraille, and S. Corréard, 2015: Mesoscale variability in the Arabian Sea from HYCOM model results and observations: impact on the Persian Gulf Water path. *Ocean Science*, **11**, 667–693, https://doi.org/10.5194/os-11-667-2015.

L'Hégaret, P., X. Carton, S. Louazel, and G. Boutin, 2016: Mesoscale eddies and submesoscale structures of Persian Gulf Water off the Omani coast in spring 2011. *Ocean Science*, **12**, 687–701, https://doi.org/10.5194/os-12-687-2016.

——, C. de Marez, M. Morvan, T. Meunier, and X. Carton, 2021: Spreading and Vertical Structure of the Persian Gulf and Red Sea Outflows in the Northwestern Indian Ocean. *Journal of Geophysical Research: Oceans*, **126**, e2019JC015983, https://doi.org/10.1029/2019JC015983.

Lian, Z., B. Sun, Z. Wei, Y. Wang, and X. Wang, 2019: Comparison of Eight Detection Algorithms for the Quantification and Characterization of Mesoscale Eddies in the South China Sea. *Journal of Atmospheric and Oceanic Technology*, **36**, 1361–1380, https://doi.org/10.1175/JTECH-D-18-0201.1.

de Marez, C., P. L'Hégaret, M. Morvan, and X. Carton, 2019: On the 3D structure of eddies in the Arabian Sea. *Deep Sea Research Part I: Oceanographic Research Papers*, **150**, 103057, https://doi.org/10.1016/j.dsr.2019.06.003.

——, X. Carton, S. Corréard, P. L'Hégaret, and M. Morvan, 2020: Observations of a Deep Submesoscale Cyclonic Vortex in the Arabian Sea. *Geophys. Res. Lett.*, **47**, https://doi.org/10.1029/2020GL087881.

McDougall, T. J., and O. A. Krzysik, 2015: Spiciness. *Journal of Marine Research*, **73**, 141–152, https://doi.org/10.1357/002224015816665589.

Meschanov, S. L., and G. I. Shapiro, 1998: A young lens of Red Sea Water in the Arabian Sea. Deep Sea Research Part I: Oceanographic Research Papers, 45, 1–13, https://doi.org/10.1016/S0967-0637(97)00018-6.

Morel, Y., J. Gula, and A. Ponte, 2019: Potential vorticity diagnostics based on balances between volume integral and boundary conditions. *Ocean Modelling*, **138**, 23–35, https://doi.org/10.1016/j.ocemod.2019.04.004.

Morrison, J. M., L. A. Codispoti, S. Gaurin, B. Jones, V. Manghnani, and Z. Zheng, 1998: Seasonal variation of hydrographic and nutrient fields during the US JGOFS Arabian Sea Process Study. *Deep Sea Research Part II: Topical Studies in Oceanography*, **45**, 2053–2101, https://doi.org/10.1016/S0967-0645(98)00063-0.

Morvan, M., X. Carton, P. L'Hégaret, C. de Marez, S. Corréard, and S. Louazel, 2020: On the dynamics of an idealised bottom density current overflowing in a semi-enclosed basin: mesoscale and submesoscale eddies generation. *Geophysical & Astrophysical Fluid Dynamics*, **114**, 607–630, https://doi.org/10.1080/03091929.2020.1747058.

Nencioli, F., C. Dong, T. Dickey, L. Washburn, and J. C. McWilliams, 2010: A Vector Geometry–Based Eddy Detection Algorithm and Its Application to a High-Resolution Numerical Model Product and High-Frequency Radar Surface Velocities in the Southern California Bight. *Journal of Atmospheric and Oceanic Technology*, **27**, 564–579, https://doi.org/10.1175/2009JTECHO725.1.

Okubo, A., 1970: Horizontal dispersion of floatable particles in the vicinity of velocity singularities such as convergences. *Deep Sea Research and Oceanographic Abstracts*, **17**, 445–454, https://doi.org/10.1016/0011-7471(70)90059-8.

Pegliasco, C., A. Chaigneau, and R. Morrow, 2015: Main eddy vertical structures observed in the four major Eastern Boundary Upwelling Systems. *Journal of Geophysical Research: Oceans*, **120**, 6008–6033, https://doi.org/10.1002/2015JC010950.

——, ——, ——, and F. Dumas, 2021: Detection and tracking of mesoscale eddies in the Mediterranean Sea: A comparison between the Sea Level Anomaly and the Absolute

Dynamic Topography fields. *Advances in Space Research*, **68**, 401–419, https://doi.org/10.1016/j.asr.2020.03.039.

Pelland, N. A., C. C. Eriksen, and C. M. Lee, 2013: Subthermocline Eddies over the Washington Continental Slope as Observed by Seagliders, 2003–09. Journal of Physical Oceanography, 43, 2025–2053, https://doi.org/10.1175/JPO-D-12-086.1.

Petersen, M. R., S. J. Williams, M. E. Maltrud, M. W. Hecht, and B. Hamann, 2013: A three-dimensional eddy census of a high-resolution global ocean simulation. *Journal of Geophysical Research: Oceans*, **118**, 1759–1774, https://doi.org/10.1002/jgrc.20155.

Prasad, T. G., M. Ikeda, and S. P. Kumar, 2001: Seasonal spreading of the Persian Gulf Water mass in the Arabian Sea. *Journal of Geophysical Research: Oceans*, **106**, 17059–17071, https://doi.org/10.1029/2000JC000480.

Prasanna Kumar, S., and T. G. Prasad, 1999: Formation and spreading of Arabian Sea high-salinity water mass. *Journal of Geophysical Research: Oceans*, **104**, 1455–1464, https://doi.org/10.1029/1998JC900022.

Queste, B. Y., C. Vic, K. J. Heywood, and S. A. Piontkovski, 2018: Physical Controls on Oxygen Distribution and Denitrification Potential in the North West Arabian Sea. *Geophysical Research Letters*, **45**, 4143–4152, https://doi.org/10.1029/2017GL076666.

Roman-Stork, H. L., and B. Subrahmanyam, 2020: The Impact of the Madden–Julian Oscillation on Cyclone Amphan (2020) and Southwest Monsoon Onset. *Remote Sensing*, **12**, 3011, https://doi.org/10.3390/rs12183011.

Sadarjoen, A. I., and F. H. Post, 2000: Detection, quantification, and tracking of vortices using streamline geometry. *Computers & Graphics*, **24**, 333–341, https://doi.org/10.1016/S0097-8493(00)00029-7.

Schneider, T., I. M. Held, and S. T. Garner, 2003: Boundary Effects in Potential Vorticity Dynamics. *Journal of the Atmospheric Sciences*, **60**, 1024–1040, https://doi.org/10.1175/1520-0469(2003)60<1024:BEIPVD>2.0.CO;2.

Schott, F. A., and J. P. McCreary, 2001: The monsoon circulation of the Indian Ocean. *Progress in Oceanography*, **51**, 1–123, https://doi.org/10.1016/S0079-6611(01)00083-0.

Shankar, D., and S. R. Shetye, 1997: On the dynamics of the Lakshadweep high and low in the southeastern Arabian Sea. *Journal of Geophysical Research: Oceans*, **102**, 12551–12562, https://doi.org/10.1029/97JC00465.

1066 Shapiro, G., and S. L. Meschanov, 1991: Distribution and spreading of Red Sea Water and
1067 salt lens formation in the northwest Indian Ocean. Deep Sea Research Part A.
1068 Oceanographic Research Papers, 38, 21–34, https://doi.org/10.1016/0198-
1069 0149(91)90052-H.
1070 Souza, J. M. a. C., C. de Boyer Montégut, and P. Y. Le Traon, 2011: Comparison between
1071 three implementations of automatic identification algorithms for the quantification and
1072 characterization of mesoscale eddies in the South Atlantic Ocean. *Ocean Science*, **7**,
1073 317–334, https://doi.org/10.5194/os-7-317-2011.
1074 Subrahmanyam, B., D. M. Heffner, D. Cromwell, and J. F. Shriver, 2009: Detection of
1075 Rossby waves in multi-parameters in multi-mission satellite observations and HYCOM
1076 simulations in the Indian Ocean. *Remote Sensing of Environment*, **113**, 1293–1303,
1077 https://doi.org/10.1016/j.rse.2009.02.017.
1078 Sun, Z., Z. Zhang, B. Qiu, C. Zhou, W. Zhao, and J. Tian, 2022: Subsurface Mesoscale
1079 Eddies Observed in the Northeastern South China Sea: Dynamic Features and Water
1080 Mass Transport. *Journal of Physical Oceanography*, **52**, 841–855,
1081 https://doi.org/10.1175/JPO-D-21-0177.1.
1082 Trott, C. B., B. Subrahmanyam, A. Chaigneau, and T. Delcroix, 2018: Eddy Tracking in the
1083 Northwestern Indian Ocean During Southwest Monsoon Regimes. *Geophysical*
1084 *Research Letters*, **45**, 6594–6603, https://doi.org/10.1029/2018GL078381.
1085 ——, ——, ——, and H. L. Roman-Stork, 2019: Eddy-Induced Temperature and Salinity
1086 Variability in the Arabian Sea. *Geophysical Research Letters*, **46**, 2734–2742,
1087 https://doi.org/10.1029/2018GL081605.
1088 Vortmeyer-Kley, R., U. Gräwe, and U. Feudel, 2016: Detecting and tracking eddies in
1089 oceanic flow fields: a Lagrangian descriptor based on the modulus of vorticity.
1090 *Nonlinear Processes in Geophysics*, **23**, 159–173, https://doi.org/10.5194/npg-23-159-
1091 2016.
1092 ——, P. Holtermann, U. Feudel, and U. Gräwe, 2019: Comparing Eulerian and Lagrangian
1093 eddy census for a tide-less, semi-enclosed basin, the Baltic Sea. *Ocean Dynamics*, **69**,
1094 701–717, https://doi.org/10.1007/s10236-019-01269-z.
1095 Wang, H., J. L. McClean, and L. D. Talley, 2021: Full Vorticity Budget of the Arabian Sea
1096 from a 0.1° Ocean Model: Sverdrup Dynamics, Rossby Waves, and Nonlinear Eddy

1097 Effects. *Journal of Physical Oceanography*, **51**, 3589–3607,
1098 https://doi.org/10.1175/JPO-D-20-0223.1.
1099 Wang, S., W. Zhu, J. Ma, J. Ji, J. Yang, and C. Dong, 2019: Variability of the Great Whirl
1100 and Its Impacts on Atmospheric Processes. *Remote Sensing*, **11**, 322,
1101 https://doi.org/10.3390/rs11030322.
1102 Weiss, J., 1991: The dynamics of enstrophy transfer in two-dimensional hydrodynamics.
1103 *Physica D: Nonlinear Phenomena*, **48**, 273–294, https://doi.org/10.1016/0167-
1104 2789(91)90088-Q.
1105 Xu, A., F. Yu, and F. Nan, 2019: Study of subsurface eddy properties in northwestern Pacific
1106 Ocean based on an eddy-resolving OGCM. *Ocean Dynamics*, **69**, 463–474,
1107 https://doi.org/10.1007/s10236-019-01255-5.
1108 You, Y., 1998: Intermediate water circulation and ventilation of the Indian Ocean derived
1109 from water-mass contributions. *Journal of Marine Research*, **56**, 1029–1067,
1110 https://doi.org/10.1357/002224098765173455.
1111 Zhan, P., D. Guo, and I. Hoteit, 2020: Eddy-Induced Transport and Kinetic Energy Budget in
1112 the Arabian Sea. *Geophysical Research Letters*, **47**, e2020GL090490,
1113 https://doi.org/10.1029/2020GL090490.
1114 Zhang, Z., W. Wang, and B. Qiu, 2014: Oceanic mass transport by mesoscale eddies.
1115 *Science*, **345**, 322–324, https://doi.org/10.1126/science.1252418.